A&A 618, A35 (2018)
https://doi.org/10.1051/0004-6361/201833558

Astronomy & Astrophysics

High-speed molecular cloudlets around the Galactic center's supermassive black hole⋆,⋆⋆

Javier R. Goicoechea[1], Jerome Pety[2,3], Edwige Chapillon[2,4], José Cernicharo[1], Maryvonne Gerin[3], Cinthya Herrera[2], Miguel A. Requena-Torres[5], and Miriam G. Santa-Maria[1]

[1] Instituto de Física Fundamental (CSIC), Calle Serrano 121, 28006, Madrid, Spain
e-mail: javier.r.goicoechea@csic.es
[2] Institut de Radioastronomie Millimétrique (IRAM), 300 rue de la Piscine, 38406 Saint-Martin-d'Hères, France
[3] Sorbonne Université, Observatoire de Paris, Université PSL, École Normale Supérieure, CNRS, LERMA, 75014, Paris, France
[4] OASU/LAB-UMR5804, CNRS, Université Bordeaux, allée Geoffroy Saint-Hilaire, 33615 Pessac, France
[5] Department of Astronomy, University of Maryland, College Park, MD 20742, USA

Received 4 June 2018 / Accepted 28 July 2018

ABSTRACT

We present 1″-resolution ALMA observations of the circumnuclear disk (CND) and the interstellar environment around Sgr A*. The images unveil the presence of small spatial scale ^{12}CO (J = 3–2) molecular "cloudlets" ($\lesssim$20 000 AU size) within the central parsec of the Milky Way, in other words, inside the cavity of the CND, and moving at high speeds, up to 300 km s^{-1} along the line-of-sight. The ^{12}CO-emitting structures show intricate morphologies: extended and filamentary at high negative-velocities ($v_{\rm LSR} \lesssim -150$ km s^{-1}), more localized and clumpy at extreme positive-velocities ($v_{\rm LSR} \gtrsim +200$ km s^{-1}). Based on the pencil-beam ^{12}CO absorption spectrum toward Sgr A* synchrotron emission, we also present evidence for a diffuse molecular gas component producing absorption features at more extreme negative-velocities ($v_{\rm LSR} < -200$ km s^{-1}). The CND shows a clumpy spatial distribution traced by the optically thin H^{13}CN (J = 4–3) emission. Its motion requires a bundle of non-uniformly rotating streams of slightly different inclinations. The inferred gas density peaks, molecular cores of several 10^5 cm^{-3}, are lower than the local Roche limit. This supports that CND cores are transient. We apply the two standard orbit models, spirals vs. ellipses, invoked to explain the kinematics of the ionized gas streamers around Sgr A*. The location and velocities of the ^{12}CO cloudlets inside the cavity are inconsistent with the spiral model, and only two of them are consistent with the Keplerian ellipse model. Most cloudlets, however, show similar velocities that are incompatible with the motions of the ionized streamers or with gas bounded to the central gravity. We speculate that they are leftovers of more massive molecular clouds that fall into the cavity and are tidally disrupted, or that they originate from instabilities in the inner rim of the CND that lead to fragmentation and infall from there. In either case, we show that molecular cloudlets, all together with a mass of several 10 $M_\odot$, exist around Sgr A*. Most of them must be short-lived, $\lesssim 10^4$ yr: photoevaporated by the intense stellar radiation field, $G_0 \simeq 10^{5.3}$–$10^{4.3}$, blown away by winds from massive stars in the central cluster, or disrupted by strong gravitational shears.

Key words. ISM: clouds – ISM: kinematics and dynamics – ISM: molecules – Galaxy: center

1. Introduction

The largest baryonic–mass reservoir feeding Galaxy nuclei is in the form of molecular gas. This reservoir is typically arranged as a circumnuclear disk (CND) or ring that rotates around the dynamical center of the Galaxy (e.g., Genzel et al. 1998; García-Burillo et al. 2014, and references therein). Associated with the radio-source Sgr A*, the center of the Milky Way (e.g., Morris & Serabyn 1996; Genzel et al. 2010) hosts a supermassive black hole (SMBH) with a mass of about $4 \times 10^6\ M_\odot$ (Schödel et al. 2002; Ghez et al. 2008; Gillessen et al. 2009). It also contains a dense cluster with more than 100 OB-type massive stars of uncertain origin (Krabbe et al. 1995; Schödel et al. 2007, 2014).

The gravitational potential of the SMBH is thought to influence the dynamics of a region out to half a parsec (pc) from Sgr A* (e.g., Trani et al. 2018). The central cavity refers to the innermost pc of the Galaxy, hosting the SMBH, the nuclear stellar cluster and prominent streamers of interstellar ionized gas. The inner edge of the CND lies at about 1.5 pc from Sgr A*. Any material orbiting inside the cavity and close to Sgr A* is expected to move at high velocities. The circular velocity in a spherically symmetric mass distribution is given by $[G\,M(r)/r]^{1/2}$, where r is the distance to the dynamical center. In this simple view, a particle following a circular orbit would acquire velocities above 150 (300) km s^{-1} at distances less than 1.0 (0.2) pc from Sgr A*.

Due to a low accretion rate onto the SMBH, the central cavity is presently quiet in terms of luminosity (e.g., Baganoff et al. 2003; Marrone et al. 2007) and does not show evidences of a strong nuclear outflow as observed in other active galaxies (e.g., Cicone et al. 2014). The interstellar medium of the cavity is pervaded by strong ultraviolet radiation (UV) fields and powerful winds from massive stars (Morris & Serabyn 1996; Genzel et al. 2010; Schödel et al. 2014). The combined action of these winds is thought to launch a roughly spherical, but currently

⋆ This paper makes use of the following ALMA data: ADS/JAO.ALMA#2013.1.01058.S. ALMA is a partnership of ESO (representing its member states), NSF (USA), and NINS (Japan), together with NRC (Canada), and NSC and ASIAA (Taiwan), in cooperation with the Republic of Chile. The Joint ALMA Observatory is operated by ESO, AUI/NRAO, and NAOJ.

⋆⋆ The full velocity range integrated line intensity images are only available at cdsarc.u-strasbg.fr (130.79.128.5) or via http://cdsarc.u-strasbg.fr/viz-bin/qcat?J/A+A/618/A35

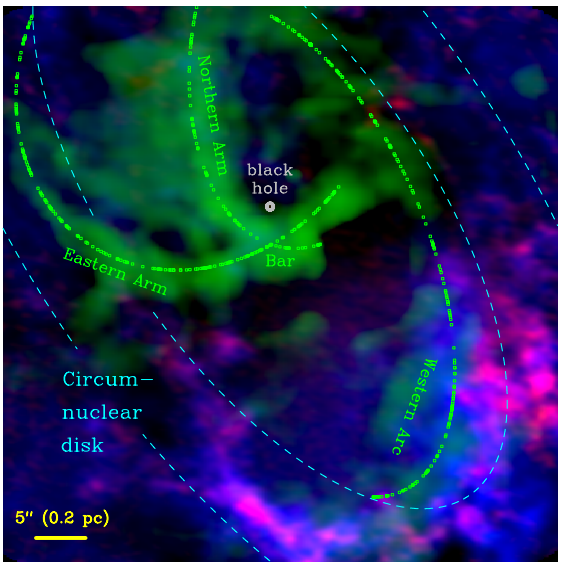

Fig. 1. Multiphase view of the central 2 pc of the Milky Way. Overlay of the ^{12}CO (J = 3–2) (blue) and H^{13}CN (J = 4–3) (red) integrated emission observed with ALMA tracing warm molecular gas in the southern lobe of the circumnuclear disk (CND). Representative inner and outer circular orbits (1.5 and 2.3 pc deprojected radii) are shown as dashed cyan curves. Closer to the supermassive black hole at Sgr A*, the dotted green curves show arms of the Keplerian elliptical orbits previously proposed to fit the motion of the ionized gas streamers (Zhao et al. 2009, and references therein) shown by the [Ne II]12.8 μm emission (green; from Irons et al. 2012). North is up and east is left.

weak, outflow of low-density ionized gas that interacts with the CND's inner rim (Geballe et al. 1987; Blank et al. 2016).

The high-density ionized gas in the cavity is organized along three conspicuous streamers, the mini-spiral, called western arc, eastern arm and northern arm (see Fig. 1), that flow around and likely toward Sgr A* (e.g., Lacy et al. 1980, 1991; Roberts et al. 1996; Paumard et al. 2004; Zhao et al. 2009, 2010; Irons et al. 2012). Two interpretations for the kinematics of the ionized gas streamers have been proposed:

i) The spiral model: nearly circular orbits with a small inward radial velocity component leading to gas moving across the western and northern arms (e.g., Serabyn & Lacy 1985; Lacy et al. 1991; Irons et al. 2012). In addition, Liszt (2003) also modeled the kinematics of the ionized gas in the eastern arm and Bar region as rotating circular rings seen nearly edge-on.

ii) The more accepted ellipse model: three families of elliptical orbits (with Sgr A* at their foci but all with different inclinations and orbital parameters) resulting in gas flowing along the streamers. Thus, this model is also called the tidally stretched cloud model (Zhao et al. 2009, and references therein). Given the observed intricate velocity patterns and complexity of the region, however, none of these kinematic models perfectly reproduce the observed velocities. Some of the discrepancies may be related to dynamical effects produced by the presence of strong magnetic fields (e.g. Morris & Serabyn 1996).

Enclosing the central cavity is a rotating ring, the CND, of warm molecular gas and dust: dashed cyan curves in Fig. 1, with deprojected inner and outer radii of about 1.5 and 2.5 pc respectively, inclined by $\simeq$70° and tilted on the sky by $\simeq$30° (Guesten et al. 1987; Jackson et al. 1993; Christopher et al. 2005; Montero-Castaño et al. 2009; Requena-Torres et al. 2012; Lau et al. 2013; Tsuboi et al. 2018). A lower excitation molecular gas component seems to extend the CND to much larger distances, out to about 10 pc, where molecular clouds there can be tidally captured, and be dragged toward the inner ring region (see e.g., Oka et al. 2011; Hsieh et al. 2017; Trani et al. 2018).

While many observations of the gas and dust toward the CND exist (e.g., Ferrière 2012, and references therein) it has been traditionally questioned whether molecular gas, the fuel to form new stars, can exist inside the cavity. The existence of molecular material in such a hostile environment: affected by enhanced UV fields, X-rays, cosmic-rays particles, stellar winds, shocks, turbulence, and strong gravity effects, was initially not expected. However, it has been more or less convincingly demonstrated recently (e.g., Yusef-Zadeh et al. 2001, 2017b; Herrnstein & Ho 2002; Goicoechea et al. 2013, 2018; Goto et al. 2014; Feldmeier-Krause et al. 2015; Moultaka et al. 2015; Ciurlo et al. 2016; Moser et al. 2017; Mills et al. 2017). Still, controversy prevails because it is not easy to assign unprojected distances from the observed molecular features to Sgr A*. The nature of the observed molecular gas emission is neither evident, interstellar: clouds or blobs, versus circumstellar: envelopes around evolved stars or young protostellar outflows and their disks (Yusef-Zadeh et al. 2017b, and references therein). High-angular resolution, velocity-resolved observations with ALMA provide new avenues to probe and characterize the molecular gas component in the vicinity of a SMBH.

Using early ALMA observations, Moser et al. (2017) presented the serendipitous detection of molecular line emission (CS, SiO, C_2H, SO, and H^{13}CO$^+$) toward the inner 20″ of the Galaxy. While most of the molecular line luminosity appears in the velocity range $v_{\rm LSR} \approx -100$ to $+100$ km s^{-1} typical of the CND, a few CS (J = 5–4) and SiO (J = 8–7) emission clumps emit at significantly higher velocities: up to $\simeq$200 km s^{-1}. Two of these clumps were previously reported in SiO (J = 5–4) by Yusef-Zadeh et al. (2013). The later authors interpreted the emission as arising in molecular outflows from embedded massive protostars. This interpretation is controversial because it implies on-going massive star formation close to Sgr A*. Instead, Moser et al. (2017) suggested that the observed features might be the dense leftovers of a disrupted molecular clump. The presence of bipolar outflows and disks around low-mass protostars within the central pc of Sgr A* has been also invoked from a recent analysis of ALMA ^{13}CO (J = 2–1) emission features, all with $|v_{\rm LSR}| < 200$ km s^{-1} (Yusef-Zadeh et al. 2017b). However, higher angular resolution and more molecular diagnostics are needed to confirm the nature of these features. In addition, previous interferometric observations were not sensitive to the presence of extended gas emission in the field (observations did not include zero- and short-spacing data).

In this work we present new ALMA ^{12}CO (J = 3–2) emission images of the region, complemented with H^{13}CN (J = 4–3) and SO (8_9–7_8) images, as well as with ^{12}CO (J = 3–2) absorption spectra toward the strong continuum source at Sgr A*. The images unveil a collection of emission features at more extreme velocities than reported before. Here we use the term *extreme* ($|v_{\rm LSR}| \gtrsim 200$ km s^{-1}) in the context of the molecular gas emission or absorption. In particular, we argue that by virtue of its extreme velocity, such gas must be located inside the cavity and close to Sgr A*. We note, however, that the emission from ionized gas inside the cavity covers an even higher velocity range: $-400 < v_{\rm LSR} < +400$ km s^{-1} (e.g., Zhao et al. 2009). As one goes closer to the SMBH, many objects including stars and small putative clouds of ionized gas in the inner $\simeq$1″ ($\simeq$0.04 pc) are known to move much faster, above 1000 km s^{-1} in the line-of-sight (e.g., Gillessen et al. 2009, 2012).

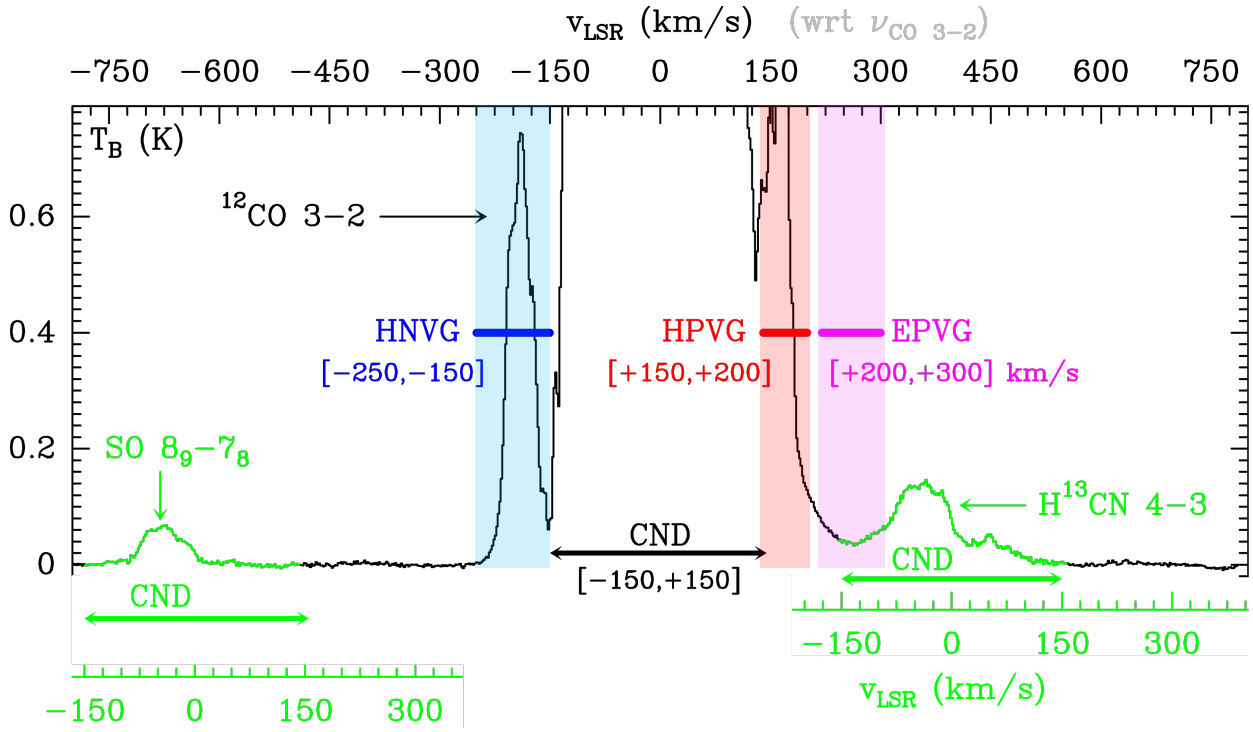

Fig. 2. ALMA plus total-power spectrum around 345.8 GHz averaged over the observed field-of-view. The black histogram shows the spectrum centered at the frequency of the CO $J = 3$–2 line (LSR velocity scale shown in the upper horizontal axis). The green spectra (and lower velocity axes) show the same for the SO 8_9–7_8 and $H^{13}CN$ $J = 4$–3 lines, both dominantly emitted from the CND in the velocity range $|v_{LSR}| < 150\,km\,s^{-1}$ (blanked out for CO). In addition to this standard velocity range, CO shows higher positive and negative velocity emission components: EPVG, HPVG, and HNVG (defined in the text) in magenta, red, and blue respectively. Owing to the similar spatial distribution of the SO and $H^{13}CN$ line emission, the CO EPVG features can be easily distinguished from the blue-shifted $H^{13}CN$ $J = 4$–3 emission in the images (see text).

This paper is organized as follows. In Sect. 2 we present the ALMA data set, calibration, and image synthesis. In Sect. 3 we summarize the main observational findings. In Sect. 4 we analyze the kinematics of the molecular gas in the CND and toward the cavity, as well as their implied masses, associated extinction, and timescales for gas photoevaporation. In Sect. 5 we discuss the possible origin of the molecular gas inside the cavity and in Sect. 6 we conclude.

2. Observations

Observations toward Sgr A* (RA (J2000) = $17^h45^m40.036^s$; Dec (J2000) = −29°00′28.17″) and the southern lobe of circumnuclear disk (CND-S, Becklin et al. 1982) were carried out using 28 12 m-array antennas as part of project 2013.1.01058.S (PI J. R. Goicoechea). The target line frequencies of this work are at 345.796 GHz (CO $J = 3$–2), 345.339 GHz ($H^{13}CN$ $J = 4$–3), and 346.528 GHz (SO 8_9–7_8). The observations consisted of a 39-pointing mosaic (see footprints in Fig. A.1). The field-of-view is 60″ × 60″. Baseline configurations from 12 to about 350 m were measured. We employed a correlator providing a resolution of 975 kHz (≃0.8 km s^{-1}) over an 1875 MHz bandwidth (≃1600 km s^{-1}), that is, the three target lines appear in the same spectrum. Figure 2 shows the frequency coverage of the observations. The observation time with the ALMA 12 m-array was ≃3 hr. ALMA executing blocks were first calibrated in CASA 4.6.0 software and then exported to GILDAS software for imaging, deconvolution, and analysis. In order to create a realistic image of the observed field and to recover any extended emission component, we added as zero-spacing a deep, fully-sampled single-dish map taken with 3 different 12-m antennas providing a beam full-width at half-maximum (FWHM) of about 18″. The total on-source time of these single-dish "total power" (TP) map was 17.4 hr. We used the on-the-fly mode with a distant reference position located at ΔRA = +258″ and ΔDec = −978″. The rms noise of the single-dish map is about 7 mK per 2 km s^{-1} channel. Figure A.1 shows the TP map used for $H^{13}CN$ ($J = 4$–3) line. Because only a single reference position was observed and the ^{12}CO emission is widespread and detectable throughout the Galactic center, we expect that residual signal in the reference position can negatively contaminate the ^{12}CO emission between $v_{LSR} \approx -100$ and +100 km s^{-1}. Thus, in this work we only discuss the ^{12}CO emission in the $|v_{LSR}| > 130\,km\,s^{-1}$ range. On the other hand, the $J = 4$–3 line of the trace species $H^{13}CN$ is faint and optically thin (cf. Christopher et al. 2005; Montero-Castaño et al. 2009; Mills et al. 2013), thus not affected by foreground/background contribution: it arises only from the CND and surroundings.

The GILDAS/MAPPING software was used to create the zero-spacing visibilities (Pety & Rodríguez-Fernández 2010) not sampled by the ALMA array. These pseudo-visibilities were merged with the interferometric (alone) observations in the UV plane. A baseline subtraction was performed also in the UV plane on the ALMA-12 m visibilities before merging. To do that, we created a linear velocity axis with 800 channels of 2 km s^{-1} width centered at the rest frequency of the ^{12}CO $J = 3$–2 line, and we made a linear fit to velocity windows devoid of molecular line emission. In particular, we excluded the [−800, −300] and [−250, +560] km s^{-1} velocity ranges (i.e., avoiding the SO, ^{12}CO, and $H^{13}CN$ line emission, see Fig. 2). Each mosaic field was then imaged and a dirty mosaic was built. The dirty image was deconvolved using the Högbom CLEAN algorithm.

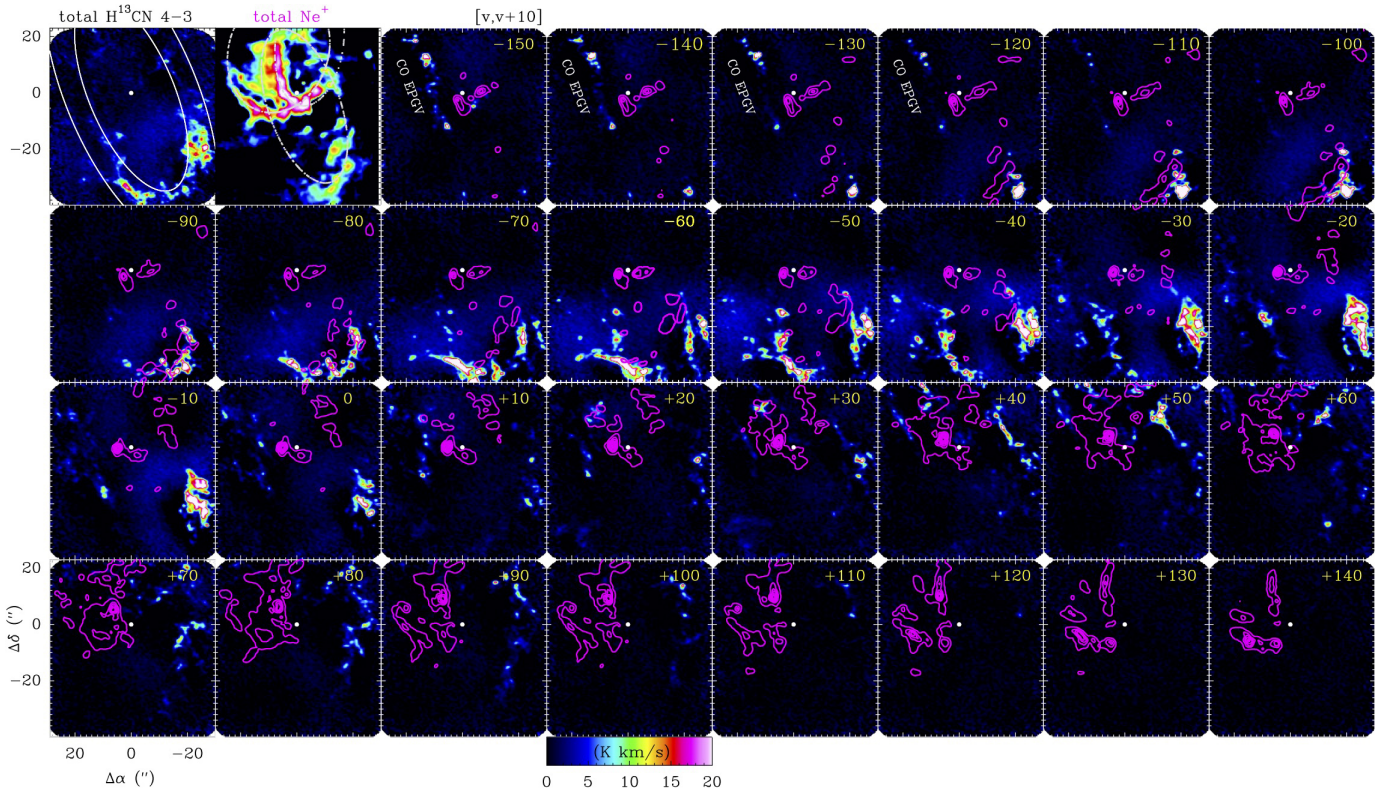

Fig. 3. ALMA $H^{13}CN$ ($J = 4$–3) and IRTF [Ne II]12.8 μm velocity channel maps from $v_{LSR} = -150$ to $+150$ km s^{-1} in steps of 10 km s^{-1}. *The two top left panels* show $H^{13}CN$ ($J = 4$–3) and [Ne II]12.8 μm total integrated line intensity maps. White curves in the $H^{13}CN$ ($J = 4$–3) map represent a CND model bounded by two rotating circular rings (with $i = 66°$, $\theta = 23°$) with inner and outer deprojected radii of 1.5 and 2.3 pc respectively. Gray curves in the [Ne II]12.8 μm map represent Keplerian elliptical orbits proposed to fit the motion of the ionized gas streamers (Zhao et al. 2009). The other panels show individual $H^{13}CN$ velocity channel maps (for intensities between 0 and 20 K km s^{-1} in linear scale) with the specific velocity interval $[v, v + 10]$ displayed at each corner. The ionized gas emission in the mini-spiral is shown in magenta contours (from Irons et al. 2012). Sgr A* is at position (0″, 0″) and is displayed with a white dot.

The resulting cubes, smoothed by integrating rectangles, to a velocity resolution of 2 km s^{-1}, were scaled from Jy/beam to brightness temperature scale using the final synthesized beam-size of 1.1″ × 0.7″. The rms noise in the final cube is ∼200 mK per resolution channel. Figures A.2 and A.4 show $H^{13}CN$ $J = 4$–3 and SO 8_9–7_8 velocity channel maps obtained from the ALMA-alone and the ALMA+TP data sets respectively. Figures A.3 and A.5 show the high and extreme positive- and negative-velocity ^{12}CO channel maps, again for the ALMA-alone and ALMA + TP data sets respectively.

3. Results

Figure 1 shows the spatial distribution of the ^{12}CO ($J = 3$–2) (blue) and $H^{13}CN$ ($J = 4$–3) (red) integrated line intensities, arising mostly from the CND, and of the [Ne II]12.8 μm line[1] (green) from ionized gas inside the cavity (from Irons et al. 2012). Figure 2 shows the ALMA+TP spectrum averaged over the observed field-of-view. The velocity axes show the velocity distribution of the three detected emission lines. The green spectra show that the $H^{13}CN$ $J = 4$–3 and SO 8_9–7_8 emission arises at velocities $|v_{LSR}| < 150$ km s^{-1} typical of the CND. Combining the spatial and velocity distributions as channel maps, Fig. 3 shows that the bulk $H^{13}CN$ ($J = 4$–3) emission is dominated by clumpy structures within the southern lobe of the CND (CND-S). The optically thin $H^{13}CN$ $J = 4$–3 emission peaks trace moderately dense molecular cores (see Sect. 4.3). As reported in previous $H^{12}CN$ observations (Christopher et al. 2005; Montero-Castaño et al. 2009), these structures follow a necklace distribution along the CND. Our higher angular resolution images, by more than a factor of four, show that the optically thick $H^{12}CN$ ($J = 4$–3) emitting structures (Mills et al. 2013; Smith & Wardle 2014) break into smaller and sharper $H^{13}CN$ ($J = 4$–3) cores. In addition, there is a diffuse gas component, meaning faint and extended, spreading around the inner edge of the CND-S. The velocity channel images in Fig. 3 visually suggest that part of this diffuse emission are lower density tails of denser structures rotating in the CND, perhaps the leftovers of cores that have been already stretched and disrupted.

But can molecular gas exist inside the CND cavity, closer to Sgr A*, for example within the central light-year (≈0.3 pc or ≈7″) of the Galaxy? ^{12}CO is a very stable molecule and about 4 orders of magnitude more abundant than $H^{12}CN$. Hence, ^{12}CO rotational emission probes very small column densities of molecular gas, hardly detectable in any other molecule, especially at velocities $|v_{LSR}| > 150$ km s^{-1}, for which the ^{12}CO emission is already faint. Indeed, the average ^{12}CO $J = 3$–2 spectrum in Fig. 2 shows additional red-shifted ^{12}CO emission components that we name *high positive-velocity gas* (HPVG; $+150 < v_{LSR} < +200$ km s^{-1}) and *extreme positive-velocity gas* (EPVG; $+200 < v_{LSR} < +300$ km s^{-1}). The associated ^{12}CO ($J = 3$–2) EPVG frequency range coincides with the

[1] The ionization potential of the Ne atom is 21.6 eV. The Ne$^+$ observations of Irons et al. (2012) have angular and velocity resolutions of 1.3″ and 4 km s^{-1} respectively, thus comparable to our ALMA images.

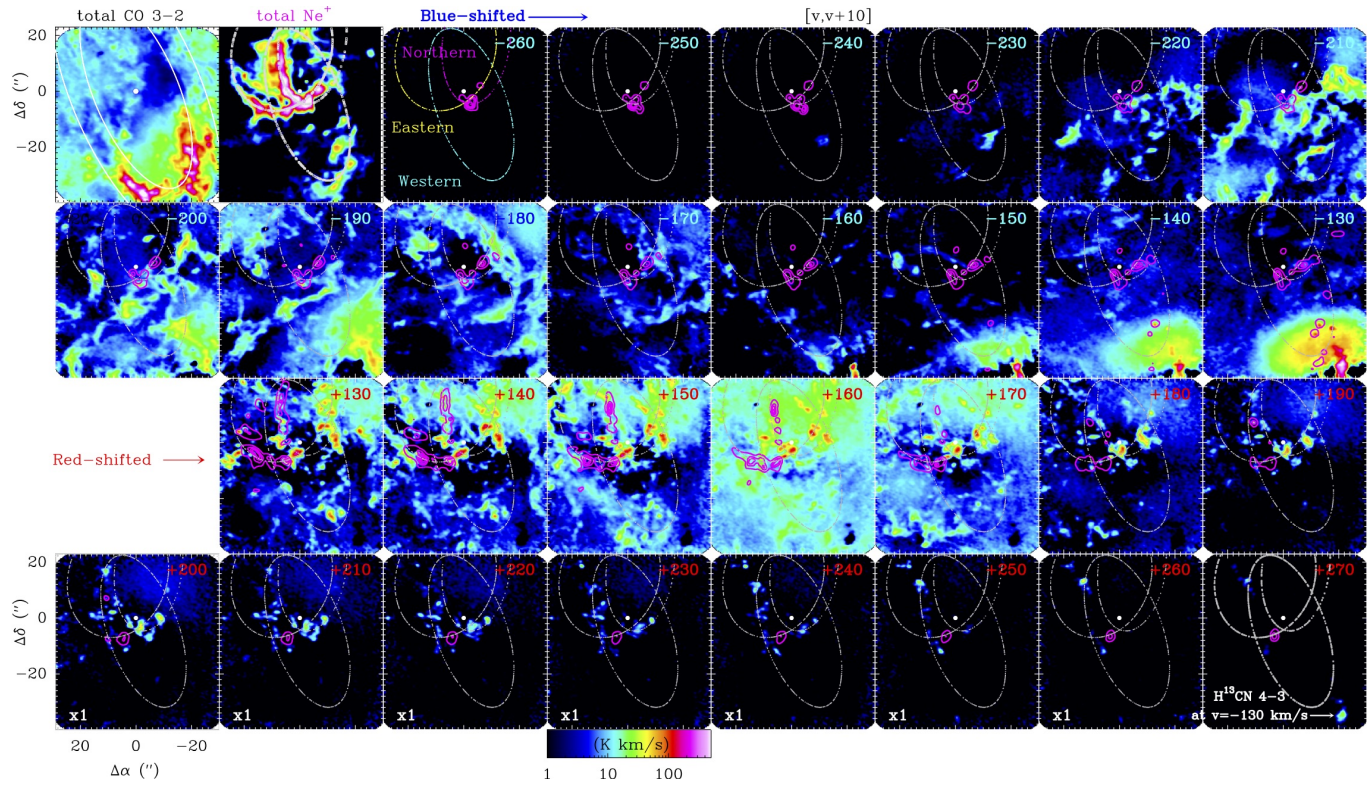

Fig. 4. ALMA high-velocity ^{12}CO (J = 3–2) and IRTF [Ne II]12.8 μm high-velocity channel maps from v_{LSR} = −260 to −120 km s^{-1} (blue-shifted) and from v_{LSR} = +130 to +280 km s^{-1} (red-shifted) in steps of 10 km s^{-1}. The *two top left panels* show ^{12}CO (J = 3–2) and [Ne II]12.8 μm total integrated line intensity maps. White curves in the ^{12}CO (J = 3–2) map represent a CND model bounded by two rotating circular rings (with i = 66°, θ = 23°) with inner and outer deprojected radii of 1.5 and 2.3 pc respectively. Gray curves represent the three Keplerian elliptical orbits proposed to fit the motion of the ionized gas streamers (Zhao et al. 2009). All the other panels show ^{12}CO velocity channel maps (for intensities between 1 and 500 K km s^{-1} in logarithm scale) with the specific velocity interval [v, v + 10] displayed at each corner. The ionized gas emission in the mini-spiral is shown in magenta contours (from Irons et al. 2012). Sgr A* is at position (0″, 0″) and is displayed with a white dot.

blue-shifted H^{13}CN emission (v_{LSR}(H^{13}CN) ≲ −100 km s^{-1}, see the spectrum in Fig. 2). Fortunately, we can easily distinguish the ^{12}CO EPVG emission from sources of blue-shifted H^{13}CN emission by taking advantage of the nearly identical spatial and velocity distribution of the H^{13}CN J = 4–3 and SO 8_9–7_8 lines (see channel maps in Figs. A.2 and A.4). In particular, the emission peaks seen in the range v_{LSR}≃+200 to +300 km s^{-1}, with respect to ^{12}CO J = 3–2, but not detected in SO 8_9–7_8, are real ^{12}CO EPVG emission features and not H^{13}CN (J = 4–3). On the other hand, there are also features that do arise from blue-shifted H^{13}CN J = 4–3 emission (v_{LSR} ≃ −100 to −140 km s^{-1}), specially toward the southern lobe of the CND because they are also detected in SO 8_9–7_8 emission (see Figs. A.2 and A.4).

Figures 4 and 5 show the collection of HPVG and EPVG clumpy emission structures detected toward the cavity interior. Owing to their small sizes (≈2″ ≲ 20 000 AU), we term these structures molecular *cloudlets*. Their (projected) location on the sky apparently agrees with the elliptical orbits of the ionized streamers inside the cavity (Fig. 4): *i*) the brightest cloudlets in the range +100 < v_{LSR} < +200 km s^{-1} resemble an extension of the eastern arm going northwest upstream, *ii*) at more extreme velocities, many EPVG cloudlets are distributed northeast of Sgr A*, apparently along the western orbit, and *iii*) close to the Bar, the ^{12}CO emission shows a bundle of emission features (structure D in Fig. 5). In the next section we compare the velocities of these cloudlets with the kinematics of the ionized gas to determine whether these spatial coincidences are fortuitous or both the molecular and the ionized streamers are linked.

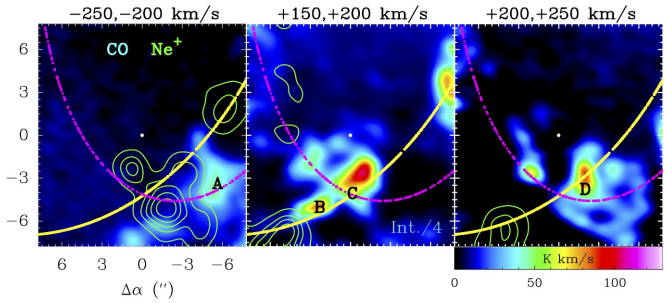

Fig. 5. Zoom into the central light-year of the Galaxy. Images show CO (J = 3–2) high-speed channel maps (*left*: v_{LSR} = −250 to −200 km s^{-1}, *middle*: v_{LSR} = +150 to +200 km s^{-1}, and *right*: v_{LSR} = +200 to +250 km s^{-1}), showing the integrated line intensity from 0 to 130 K km s^{-1}, and revealing molecular gas close to Sgr A*. Green contours show the ionized gas emission (Irons et al. 2012). The yellow and magenta tracks are segments of the Keplerian elliptical orbits along the eastern and northern arms respectively (Zhao et al. 2009).

In Fig. 6 we identify the location and extract the spectra of several ^{12}CO HPVG and EPVG cloudlets: emission peaks that show an isolated spectral component in a given velocity range; Gaussian line fit parameters are tabulated in Table B.1. Despite their small sizes, their line-profiles are very broad, typically $\Delta v \simeq$ 25–40 km s^{-1}, suggesting strong tidal shear and turbulence dissipation. We checked that their position and velocities do not coincide with the proplyd and low-mass protostar outflow candidates reported by Yusef-Zadeh et al. (2017a,b) inside the cavity.

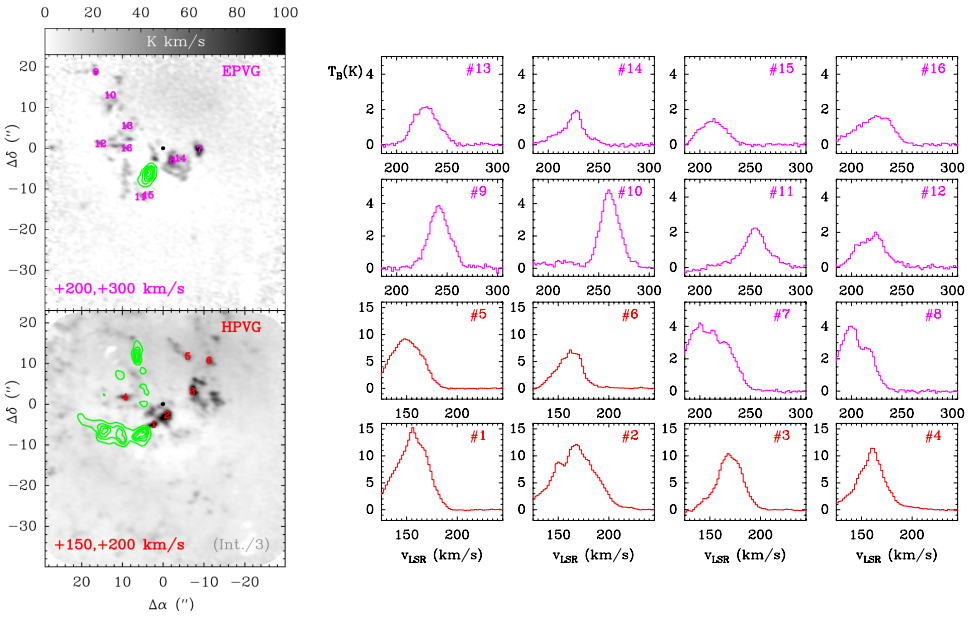

Fig. 6. *Left:* EPVG (magenta, *top*) and HPVG (red, *bottom*) molecular cloudlets, numbered, for which we have extracted their ^{12}CO $J = 3$–2 spectra. The gray images show the ^{12}CO $J = 3$–2 line emission integrated in the velocity interval displayed in each panel. The green contours shows the ionized gas emission in the same velocity range ([Ne II]12.8 μm line from Irons et al. 2012). Sgr A* is displayed with a black dot. *Right:* EPVG (magenta) and HPVG (red) cloudlet spectra. The numbers correspond to their position in the *left panels*. In each panel the velocity axis has a common width of 125 km s^{-1}. Gaussian line fit parameters are tabulated in Table B.1.

Only the ^{12}CO HPVG cloudlet #4 coincides with the SiO emission "Clump 2" previously detected by Yusef-Zadeh et al. (2013) and Moser et al. (2017) southwest of IRS 1W star cluster.

Although we added the TP data to recover the extended molecular emission filtered out by the interferometer, the bulk of the ^{12}CO clumpy emission in the EPGV range comes from small-scale structures detected by ALMA interferometer alone. This emphasizes their compact sizes (Fig. A.3). In general, the TP data adds a more extended and faint gas component that surrounds the H^{13}CN cores in the CND, and also the ^{12}CO cloudlets at higher velocities. In the Appendix we show TP and ALMA-alone velocity channel maps.

In addition to the positive-velocity emission components, we also detect widespread ^{12}CO emission at high negative-velocities ($v_{\rm LSR} < -150$ km s^{-1}, see Fig. 4). These structures are more extended and show very filamentary morphologies. Their exact location, their distance to Sgr A*, is much more difficult to determine because this is also the velocity range of the so-called foreground high negative-velocity gas (HNVG; $-200 \lesssim v_{\rm LSR} \lesssim -150$ km s^{-1}) clouds (e.g., Guesten & Downes 1981; Zhao et al. 1995). These foreground clouds are not related to the CND or Sgr A* (see Sect. 4.5). Nevertheless, some of the observed blue-shifted ^{12}CO cloudlets seem to lie inside the cavity because they overlap or closely delineate the shape of some ionized gas features, for example structure A in Fig. 5 near the Bar region where the northern and eastern arms intersect.

4. Analysis

4.1. CND kinematics: bundle of non-uniformly rotating orbits

As common in the literature, we model the CND kinematics as a set of uniformly rotating rings (Guesten et al. 1987; Jackson et al. 1993). We adopt a distance of 8300 pc to Sgr A* (Genzel et al. 2010). The sketch in Fig. 7 summarizes the coordinate system. Assuming circular velocities, with ϕ the azimuth angle in the orbit plane, the projected coordinates on the sky and those of the orbital plane are related by the inclination angle i between the two planes, and by the angle θ between the north axis and the intersection of the orbital and sky planes. The observed line-of-sight velocity ($v_{\rm LSR}$) at a given position of the projected orbit is given by $v_{\rm LSR}(r) = v_\phi(r) \sin i \cos\phi$,

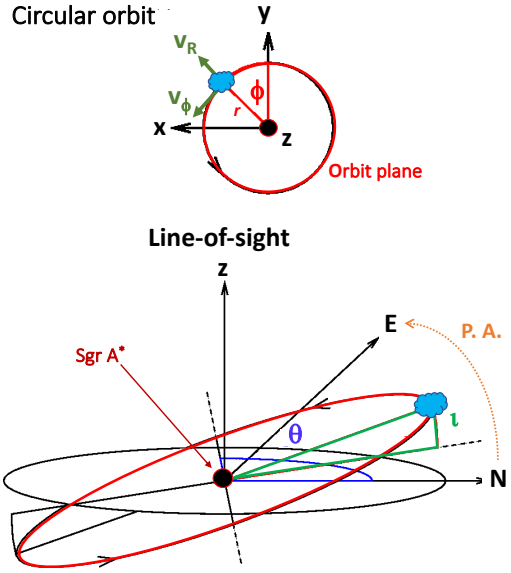

Fig. 7. Cloudlet in a circular orbit. Orbit plane: the position of a cloudlet is determined by the azimuth angle ϕ and the deprojected distance r to Sgr A*. The circular (tangential) velocity is v_ϕ. A small radial velocity $v_{\rm R}$ will make the cloudlet spiral outward ($v_{\rm R} > 0$) or inward ($v_{\rm R} < 0$). Plane of the sky: the orbit appears to an observer as an ellipse characterized by the inclination angle i between the two planes, and by the angle θ between the north axis and the intersection of the orbital and sky planes. PA refers to the position angle on the sky, from the north axis to the east axis, used in Fig. 8 and in the text.

where v_ϕ is the circular (tangential) velocity in the orbital plane (Rogstad et al. 1974) and where we take into account that the source systemic velocity is $v_{\rm SYS} = 0$ km s^{-1}. The circular velocity of a particle moving in a gravitational potential is determined by the enclosed mass at a given radius r from the dynamical center, with $v_\phi = [G\,M(r)/r]^{1/2}$ and $M(r) = M_{\rm SMBH} + M_\star(r)$. This expression accounts for the mass of the SMBH at Sgr A* ($M_{\rm SMBH} \simeq 4.2 \times 10^6\,M_\odot$; Schödel et al. 2002; Ghez et al. 2008; Gillessen et al. 2009) and for the accumulated mass of the nuclear stellar cluster at a given radial distance from the center $M_\star(r)$ (e.g., Genzel et al. 2010; Schödel et al. 2014). Here we follow Irons et al. (2012) and use a

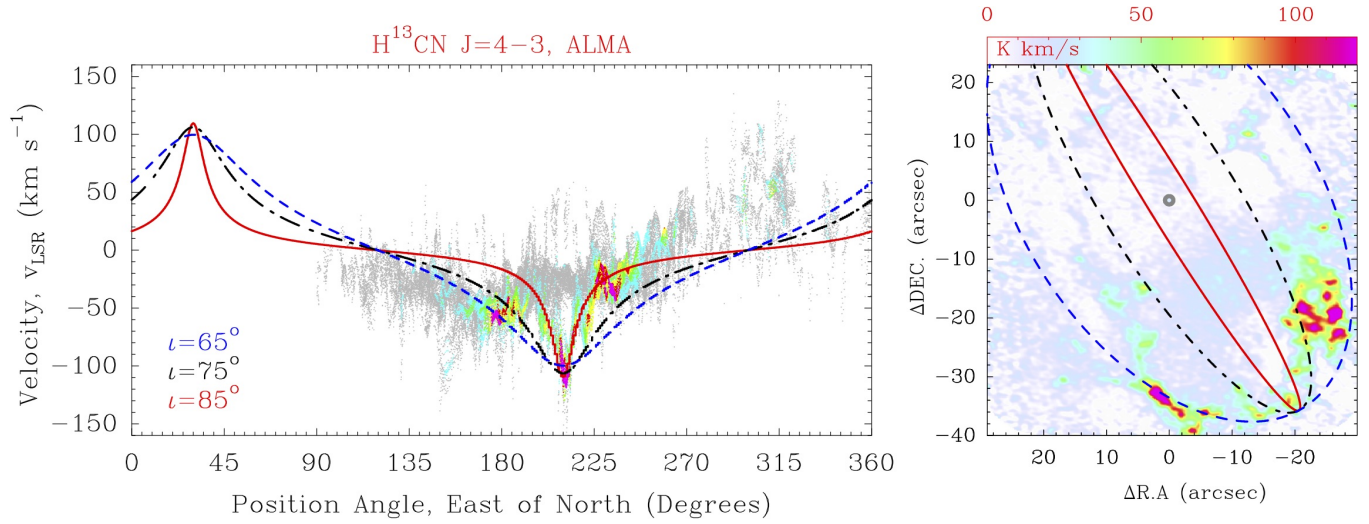

Fig. 8. Mean $H^{13}CN$ ($J = 4$–3) velocities and models of rotating circular rings for the CND. *Left*: observed velocities as a function of position angle on the sky (from north to east). Colors represent the same intensity scale as in the integrated line intensity image shown in the right panel. Curves show models of rotating, tilted rings with a circular velocity $v_\phi = 110$ km s^{-1}, $\theta = 30°$, and different inclination angles i. *Right*: integrated intensity map and resulting orbits (with a deprojected radius of 1.7 pc in this example).

simplified mass distribution $M_\star(r) \simeq m_\star \cdot r^{1.2}$ with r in pc and $m_\star = 10^6\,M_\odot$ (Genzel et al. 2010). In order to improve the fit, we allowed an ad hoc parameter β, from 0 to 1, so that the actual circular velocity is $v_\phi \cdot \beta$. For $\beta < 1$, this is equivalent to decreasing the enclosed mass but it can also be interpreted as a brake mechanism due to friction, perhaps as a result of enhanced magnetic fields in the CND.

Figure 8 shows synthetic rotation curves plotted over the $H^{13}CN$ ($J = 4$–3) intensity-weighted mean velocities as a function of position angle on the sky (PA from north to east, see sketch in Fig. 7). Most of the bright $H^{13}CN$ ($J = 4$–3) emission can be bracketed by models of circular orbits tilted by $\theta \simeq 30°$ and i from 65° to 75° but with indications of orbits of higher inclination, $i \simeq 85°$. Our inferred i and θ angles are slightly larger than previous estimations (e.g., Guesten et al. 1987; Jackson et al. 1993; Smith & Wardle 2014) and show that, even for the typical CND bright emission velocities ($|v_{LSR}| \lesssim 100$ km s^{-1}) the gas motion is better described by a bundle of orbits that cover different inclinations instead of a co-planar set of circular orbits. In agreement with previous low-resolution observations (Guesten et al. 1987; Jackson et al. 1993), the required circular velocity is $v_\phi = 100$–110 km s^{-1} ($\beta \simeq 0.8$–0.9). In the inner edge of the CND, this circular motion implies a rotational period $\tau_{rot}(\varphi)$ of $\lesssim 10^5$ yr. Figure 8 also demonstrate that a single rotating structure can't fit the $H^{13}CN$ emission from the CND (see also Martín et al. 2012).

It is also clear that several structures in the CND depart from a uniformly rotating circular motion. In particular, the emission structure emitting at $v_{LSR} \simeq +40$ to $+100$ km s^{-1} (PA $\simeq 300°$–$315°$ in Figs. 3 and 8). This component may be related to the $+80$ km s^{-1} OH-absorption streamer detected by Karlsson et al. (2015) and that likely follows a specific trajectory. In addition, Fig. 8 shows the contribution of the diffuse $H^{13}CN$ emission component that spreads around the inner edge of the CND-S (gray color shaded areas in Fig. 8). Most positions and velocities associated to this component cannot be fitted by circular orbits either.

With the [Ne II] 12.8 μm cube in hand, we also analyze the kinematics of the ionized gas adjacent to the CND-S, that is, the western arc. Globally, the ionized and the molecular gas follow the same velocity pattern (PA from $\simeq 170°$ to 230° in Fig. 8). In particular, the channel maps $v_{LSR} \approx -100$ to -50 km s^{-1} in Fig. 3 show the smooth transition between the ionized gas and the $H^{13}CN$ emission, confirming previous suggestions that the western arc is the inner ionized rim of the UV-irradiated CND-S lobe (Zhao et al. 2009; Irons et al. 2012).

4.2. Plausible cloudlet motions inside the central cavity

We investigate the possible motions of the molecular cloudlets seen toward the central cavity. We start by confronting the spiral and the ellipse models of the orbiting ionized streamers. We compare models predictions with the ^{12}CO high-speed $|v_{LSR}| > 150$ km s^{-1} emission, and with the lower velocity range typical of the CND, v_{LSR} from -150 to $+150$ km s^{-1}, for the $H^{13}CN$ emission. In some instances, the ionized and the molecular gas are directly related, for example the western arc and the CND-S, so that this comparative analysis is justified.

4.2.1. The spiral model

This is an extension of the idealized CND circular motion of previous section but the molecular gas can now have a small inward radial velocity component $v_R(r)$ toward Sgr A* (Fig. 7). Hence, the gas originally rotating in the CND slowly spirals inwards the cavity until stretched, disrupted, or photodissociated and ionized by the strong UV radiation field from the nuclear star cluster. The observed gas velocity of such a spiral will be

$$v_{LSR}(r) = v_\phi(r)\,\sin i \cos\phi + v_R(r)\,\sin i \sin\phi. \quad (1)$$

Irons et al. (2012) argue that the kinematics of the ionized gas in the western arc and northern arm can be explained, as a single structure, if the gas moves along circular orbits with a small radial velocity $v_R(r) = (a/r)\,v_\phi(r)$, that is, increasing closer to Sgr A*, and resulting in a single one-armed spiral density wave. Their best model is for $\theta = 23°$, $i = 66°$, and $a = -0.06$ pc, thus

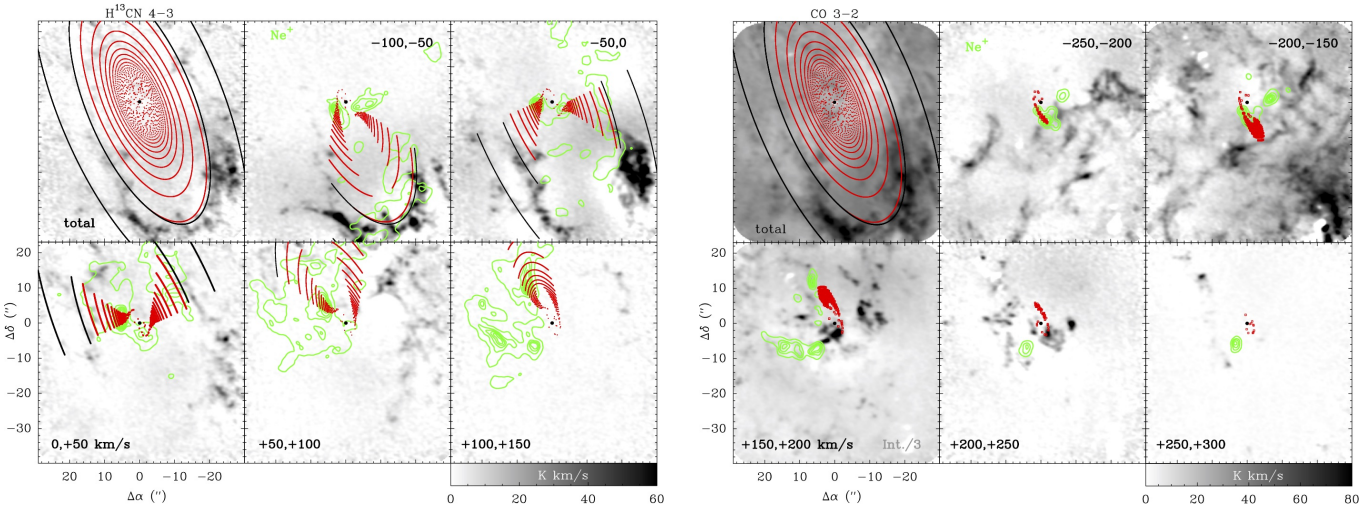

Fig. 9. Modeled spiral orbits (red segments) over $H^{13}CN$ ($J = 4$–3) channel maps at typical CND velocities v_{LSR} from −100 to +150 km s^{-1} (*left*) and over higher-velocity ^{12}CO ($J = 3$–2) channel maps (*right*), both in steps of 50 km s^{-1}. The spirals are nearly circular orbits ($i = 66°$ and $\theta = 23°$) with a small inward radial velocity component ($a = -0.06$ pc, see text) proposed by Irons et al. (2012) to explain the motion of the ionized gas (shown in green contours) across the northern arm and western arc. Black curves represent a CND model bounded by two rotating circular rings with inner and outer deprojected radii of 1.5 and 2.3 pc respectively. Sgr A* is displayed with a black dot.

implying $v_R \simeq 4$ km s^{-1} at the inner edge of the CND. In Fig. 9 we show this spiral model applied to different velocity channels of the molecular emission. We just show one spiral, moving in a single plane, as representative of a family of similar orbits. Only at low velocities ($|v_{LSR}| < 100$ km s^{-1}; left panels in Fig. 9) there is possible agreement between some of the observed $H^{13}CN$ emission features and the synthetic spiral tracks. These features are consistent with molecular gas leaving the CND and finding its way inward the cavity through nearly circular orbits partially protected from the strong stellar UV radiation. We propose that the trail of such spirals could contribute to the more diffuse and extended emission as well.

The timescale required for a cloudlet to spiral from the inner edge of the CND to 5″ from Sgr A* (a deprojected radius of 0.2 pc) would be $\simeq 1.5 \times 10^5$ yr. Therefore, such a cloudlet will turn several times around Sgr A* before reaching this radius. For molecular cloudlets, such timescales mean that they will be likely photoevaporated before reaching the very central region unless their column densities are large enough to provide some UV-shielding (see Sect. 4.4). Indeed, the spiral model cannot fit the kinematics of the ^{12}CO cloudlets at extreme velocities ($|v_{LSR}| > 200$ km s^{-1}) because it only predicts such elevated velocities close to Sgr A* and not throughout the cavity as observed (see right panels in Fig. 9).

4.2.2. The ellipse model

The line-of-sight velocity of a cloudlet following a Keplerian elliptical orbit with the SMBH at one focus is:

$$v_{LSR} = \sqrt{GM/p}\,[(e + \cos f)\cos\omega \sin(\pi - i) \quad (2)$$

$$-\sin f \sin\omega \sin(\pi - i)], \quad (3)$$

where $p = a(1 - e^2)$ (a is the ellipse semimajor axis and e the eccentricity), ω is the argument of periapsis, i is the orbit inclination angle (defined as in the previous section), and f is the angle of true anomaly defined as $cos\, f = p/(e \cdot r - 1/e)$ (with r the radial distance from the orbiting cloudlet to Sgr A*, see Fig. 10).

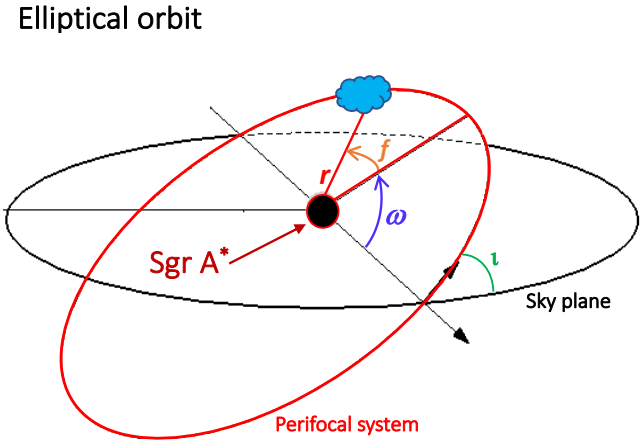

Fig. 10. Cloudlet in an elliptical orbit. In the perifocal frame, with Sgr A* in one of the ellipse focus, the position the cloudlet is determined by the true anomaly angle f. In the plane of the sky, the velocity measured along the line-of-sight depends on the argument of periapsis ω and on the inclination angle i between the orbit and the sky planes.

The red segments in Fig. 11 show the expected location and v_{LSR} velocities of the three families of Keplerian orbits that better fit the spatial distribution and velocities of the ionized gas streamers, the standard model (see Table 5 of Zhao et al. 2009, for the orbital parameters). The green contours show the [Ne II] 12.8 μm emission in the same velocity bins. At low negative-velocities, typical of the CND-S lobe, the molecular gas matches the kinematics of the ionized western arc (chanel maps $v_{LSR} = -100$ to 0 km s^{-1} in Fig. 11 left). Other than that, there is no other major correspondence between the low velocity $H^{13}CN$ and the ionized gas emission toward the cavity.

The right panels in Fig. 11 show the predictions of the ellipse model, red segments, over the higher velocity ($|v_{LSR}| > 150$ km s^{-1}) ^{12}CO emission. Despite the apparent match between the position of several cloudlets along the ellipse orbits, the velocities of most ^{12}CO cloudlets are not consistent with the velocities of the orbiting ionized streamers. In particular,

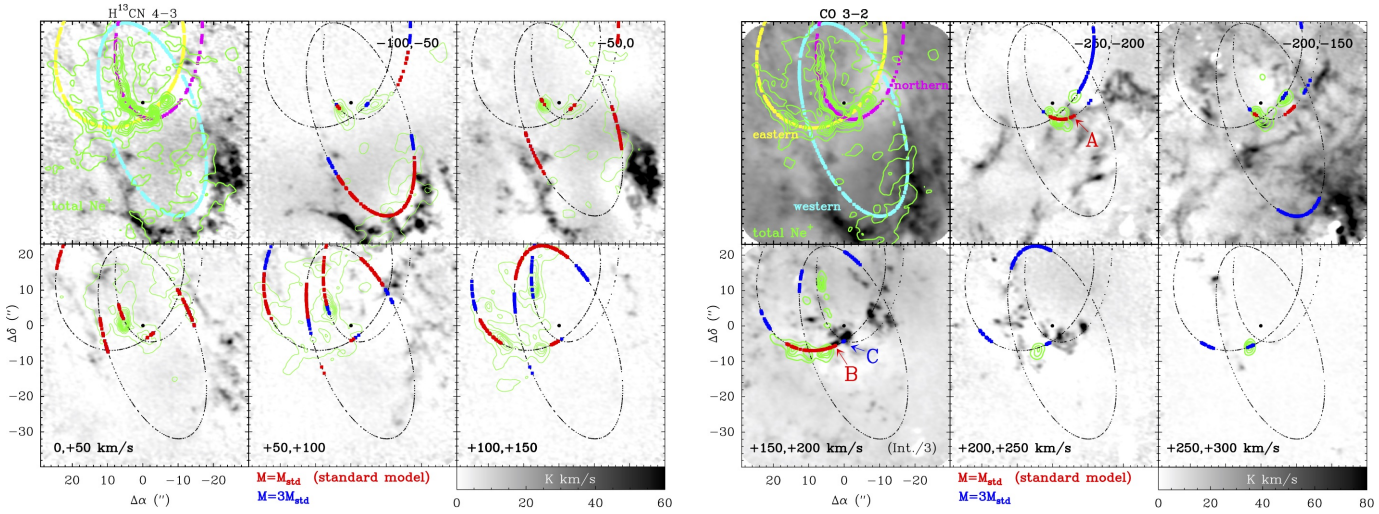

Fig. 11. Modeled Keplerian ellipse orbits over $H^{13}CN$ ($J = 4$–3) channel maps at typical CND velocities v_{LSR} from −100 to +150 km s^{-1} (*left*) and over higher-velocity ^{12}CO ($J = 3$–2) channel maps (*right*). Green contours show the [Ne II]12.8 μm emission from ionized gas streamers (Irons et al. 2012). The red orbit segments show the expected location of the gas according to the best-fit orbital parameters of Zhao et al. (2009) for the ionized gas (standard mass model). The blue orbit segments are for a model in which the dynamical mass (M in Eq. (2)) is multiplied by 3.

the HPVG cloudlets seen as a prolongation of the eastern arm, in the north-west direction, appear at high positive-velocities $v_{LSR} = +150$ to $+200$ km s^{-1} channel map, whereas the model predicts, and the ionized gas is observed at, negative velocities. Similarly, the EPVG cloudlets seen along the western orbit, $v_{LSR} = +200$ to $+300$ km s^{-1} channel maps, appear at much higher positive velocities than those predicted by the model. Only the molecular structures labeled as A and B, including HPVG cloudlet #1, show agreement in both position and velocity along the northern and eastern Keplerian orbits. In the ellipse model, these orbit positions are located at a deprojected distance of ≃0.3 pc (≃1 lyr) from Sgr A*.

To test the impact of a higher central dynamical mass in the orbit velocities, in Fig. 11 we also show a more extreme model in which we increase the enclosed mass (M in Eq. (2)) by a factor of 3, thus increasing the gas velocities along the orbits (blue segments in Fig. 11). Only for the molecular structure C, including HPVG cloudlet #2, the CO emission matches the predictions well. However, according to our current knowledge of the SMBH and stellar cluster masses (Genzel et al. 2010; Schödel et al. 2014) this model is less realistic than the standard one.

4.3. Molecular gas densities, masses, and extinction

We estimate the ^{12}CO- and $H^{13}CN$-emitting gas column densities and masses over the different velocity intervals. We assume a single rotational temperature (T_{rot}) and a Boltzmann distribution of rotational levels. If the abundance of the species s with respect to H nuclei is known ($x(s) = N(s)/N_H$) one can estimate the total $N_H = N(H + 2H_2)$ column density of molecular gas for each velocity range, and also the visual extinction along a given line-of-sight $A_V \simeq N_H\,(\mathrm{cm^{-2}})/1.9 \times 10^{21}$ mag for standard interstellar grains. We note the much higher critical density (n_{cr}) for collisional excitation of $H^{13}CN$ rotational transitions compared to those of CO: $n_{cr}(H^{13}CN\ 4\text{–}3) \simeq 10^8$ cm^{-3} versus $n_{cr}(CO\ 3\text{–}2) \simeq 4 \times 10^4$ cm^{-3}. For gas densities $n_H \ll n_{cr}$, this leads to subthermal emission, thus low rotational temperatures ($T_{rot}(H^{13}CN) \ll T_k$) but it does not necessarily mean the the $H^{13}CN$-emitting gas is very dense, as it is often assumed in the literature of the Galactic center.

The $H^{12}CN$ abundance is well constrained by chemical models to $x(H^{12}CN) \approx 5 \times 10^{-9}$ (Boger & Sternberg 2005). Here we take $x(H^{13}CN) = 10^{-8}/25$ to accommodate the higher metallicity and low isotopic ratio $^{12}C/^{13}C = 25$ in the Galactic center (Mezger et al. 1996; Martín et al. 2012). We integrate the column density equations for optically thin line emission

$$N_{thin}(s) = 8\pi \frac{\nu^3}{c^3} \frac{Q\,(T_{rot})}{g_u\,A_{ul}} \frac{1}{1 - e^{E_u/kT_{rot}}} \frac{\int T_B(\mathrm{v})\,d\mathrm{v}}{J(T_{rot}) - J(T_{bg})}\ \ (\mathrm{cm^{-2}}), \tag{4}$$

over different areas and velocity ranges. In this equation $J(T) = T^*/(e^{T^*/T} - 1)$ is the equivalent brightness temperature, with $T^* = E_u/k$ T. The integral term represents the line intensity in K km s^{-1} and T_{bg} is the cosmic microwave background temperature. If the emission is slightly optically thick, line opacity $\tau_{emi} \simeq 1$, one can add an optical depth correction $N(s) = N_{emi}(s) \cdot \tau_{emi}/(1 - e^{-\tau_{emi}})$, where

$$\tau_{emi} = -\ln\left[1 - \frac{T_B^{Peak}}{J(T_{rot}) - J(T_{bg})}\right], \tag{5}$$

can be estimated from observations.

For the expected range of rotation temperatures[2] $T_{rot}(H^{13}CN) = 20$ to 100 K, we determine an H_2 mass of 700–1100 $M_\odot$ in the CND-S lobe ($|v_{LSR}| < 100$ km s^{-1}). For a mean core diameter in the CND of 0.15–0.25 pc (see also Christopher et al. 2005; Lau et al. 2013), we estimate an average core gas density of $\langle n_H \rangle \simeq 10^5$ cm^{-3} and density peaks of $n_H \simeq 2n(H_2) \simeq (3\text{–}4) \times 10^5$ cm^{-3}. These values would be a factor of about five higher if $x(HCN) \simeq 2 \times 10^{-9}$, the lower limit of chemical model predictions (Boger & Sternberg 2005).

Our inferred masses and densities for the molecular cores in the CND roughly agree, actually they are up to a factor ten lower, with those derived from local LVG models of optically thick $H^{12}CN$ lines (Mills et al. 2013; Smith & Wardle 2014).

[2] $T_{rot}(H^{12}CN) = 43 \pm 6$ K from $H^{12}CN$ $J = 6$–5 to 8–7 line observations (Goicoechea et al. 2018).

Our simple estimates from $H^{13}CN$ ($J = 4$–3) agree more with the densities inferred from the less abundant species HCO^+ (Mills et al. 2013). This suggests that for abundant high-dipole moment molecules, in addition to mid-IR pumping, line optical depth effects determine the emergent line intensities and their spatial distribution. In particular, the $H^{12}CN$ emission that arises from inside the cores can be scattered by lower density envelopes and dispersed over larger areas than the true spatial extend of the cores, for example traced by $H^{13}CN$. This is seen in observations (Cernicharo & Guelin 1987) and is explained by more accurate non-local radiative transfer models (Gonzalez-Alfonso & Cernicharo 1993; Goicoechea et al. 2006).

In any case, our analysis and the more detailed excitation analyses demonstrate that the densities of the CND cores are lower, by approximately two orders of magnitude, than the local Roche density: several 10^7 cm^{-3}. This supports that the CND cores are unstable against tidal shear from the central mass (Guesten et al. 1987; Jackson et al. 1993; Requena-Torres et al. 2012; Lau et al. 2013; Mills et al. 2013; Smith & Wardle 2014). Hence, they will disaggregate, creating streamers and ring segments, and have difficulty forming new stars. This conclusion, however, does not immediately imply that the entire CND is a transient entity itself (see Sect. 5).

The mass for the CND-S lobe estimated from $H^{13}CN$, $\approx 10^3$–10^4 $M_\odot$ is lower than previous studies that presume that cores are massive enough to be self-gravitating. In other words, that their broad line-widths, $\Delta v \approx 20$–30 km s^{-1}, are caused by virialized motions and not by turbulence and strong tidal shear (e.g., Christopher et al. 2005; Montero-Castaño et al. 2009). Instead, they agree more with detailed HCN and HCO^+ excitation and line radiative transfer analyses (Mills et al. 2013; Smith & Wardle 2014), and with the dust continuum emission (Telesco et al. 1996; Latvakoski et al. 1999; Etxaluze et al. 2011; Lau et al. 2013) although grain models also have caveats: composition, size distribution, etc.

Following the single $T_{\rm rot}$ method summarized in Eq. (4) we also estimate the column densities associated with the high velocity ^{12}CO cloudlets detected inside the cavity. We assume a uniform CO abundance of $x(^{12}CO) = 2 \times 10^{-5}$ and $T_{\rm rot} = 100$ K. This $T_{\rm rot}$ value has been derived from spatially unresolved observations of high positive-velocity CO $J = 5$–4 to $J = 10$–9 line emission wings (Goicoechea et al. 2018). Under strong far-UV (FUV; stellar photons with $5 < E < 13.6$ eV) irradiation conditions ($G_0 \geq 10^4$ in Habing units) state-of-the-art photochemical models predict ^{12}CO abundances ranging from $x(^{12}CO) \simeq 10^{-6}$ at low visual extinctions A_V (<1–2 mag), to $x(^{12}CO) \simeq 10^{-4}$ in well shielded molecular cloud interiors (e.g., Joblin et al. 2018; Goicoechea et al. 2018). Here we take the mean value and multiply by 2 to account for the higher metallicity of the Galactic center (Mezger et al. 1996; Bolatto et al. 2013). Because we estimate $\tau_{\rm emi}(^{12}CO\ J = 3$–$2) \gtrsim 1$ toward several cloudlets, we allow for an opacity correction factor estimated from the observed line peak temperature (Eq. (5)). Only toward the CND, at lower $v_{\rm LSR}$, the ^{12}CO emission is $\tau_{\rm emi} \gg 1$.

For the EPVG component ($v_{\rm LSR} = +200$ to $+300$ km s^{-1}) we derive extinction peaks of $A_V \simeq 1.5$–1.8 mag toward 3 EPVG cloudlets and a total H_2 mass of 6–12 $M_\odot$. This value includes the ^{12}CO EPVG cloudlets and the more extended diffuse emission component, $A_V \simeq 0.1$–0.3 mag, detected at these velocities. The typical cloudlet sizes are roughly 2″. This translates into a few gas density peaks of $n_{\rm H} \simeq (1.2$–$2.5) \times 10^4$ cm^{-3}, thus very far from the critical density, $n_{\rm Roche} \simeq 6 \times 10^{10}\,(0.1\,{\rm pc}/r)^3$ (cm^{-3}) needed to overcome the tidal shear in the central pc (Morris & Serabyn 1996; Genzel et al. 2010). These cloudlets are thus stretched and many of them violently disrupted into smaller constituents of lower mass and A_V. Figure 12 (right) shows a map of the approximate visual extinction produced by the EPVG cloudlets obtained by assuming a uniform ^{12}CO abundance and $T_{\rm rot}$.

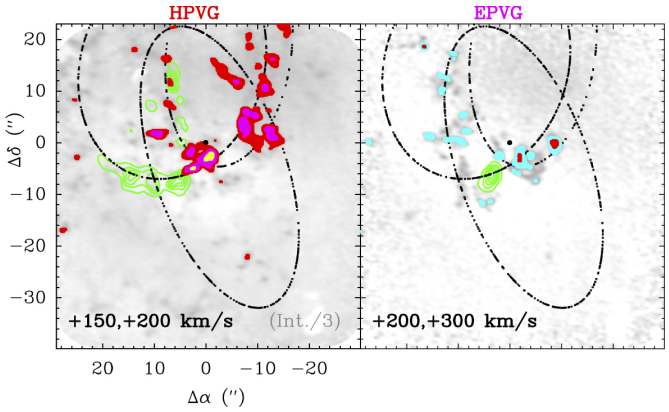

Fig. 12. Approximate visual extinction (A_V) map produced by the HPVG and EPVG cloudlets and obtained from ^{12}CO assuming a uniform abundance $x(^{12}CO) = 2 \times 10^{-5}$ and a single rotational temperature $T_{\rm rot}(^{12}CO) = 100$ K (see text). The color code shows the estimated extinction peaks: $A_V \approx 6$–9 (yellow), $A_V \approx 3$–6 (magenta), $A_V \approx 1.5$–3 (red), and $A_V \approx 0.6$–1.5 mag (cyan, shown only in the *right panel*). The gray images show the ^{12}CO $J = 3$–2 line emission integrated in the velocity interval displayed in each panel. The green contours shows the ionized gas [Ne II]12.8 μm emission at the same velocities (Irons et al. 2012).

A similar analysis of the velocity range $v_{\rm LSR} = +150$ to $+200$ km s^{-1} leads to an average visual extinction value of 0.6–1.0 mag through the field, and several ^{12}CO HPVG cloudlets with visual extinction peaks of $A_V \simeq 3$–9 mag (Fig. 12, left). This implies the presence of a few cloudlets with enough shielding against strong FUV radiation fields. The estimated H_2 mass in this velocity interval is 45–90 $M_\odot$, but it includes the possible contribution from background emission sources not related to Sgr A* (see Sect. 4.5). Our estimated extinction and mass values inside the cavity have to be multiplied by about two if $T_{\rm rot}(CO) = 200$ K and reduced by a factor five if the assumed CO abundance is increased to $\sim 10^{-4}$.

4.4. FUV attenuation and photo-dissociation timescales

The near-infrared (NIR) extinction toward Sgr A* is $A_{Ks} \approx 3$ ($\lambda_{Ks} = 2.2$ μm, Genzel et al. 2010; Schödel et al. 2010). This value includes $A_V \approx 30$ magnitudes of visual extinction ($\lambda_V = 0.55$ μm) produced by cold foreground clouds in the line-of-sight toward the Galactic center (e.g., Moneti et al. 2001). Combining Paschen-α line ($\lambda_{P\alpha} = 1.87$ μm), 6 cm radiocontinuum, and mid-infrared (MIR) dust emission observations, Lau et al. (2013) presented maps of the MIR extinction ($\lambda_{\rm MIR} = 19.7$ μm) intrinsic to the CND and cavity. In these maps it is evident that the local MIR extinction is greater along the western arc than toward the central cavity: it peaks at the CND-S lobe, it is low along the ionized streamers, and it rises again close to Sgr A* (north-west).

Ciurlo et al. (2016) presented a ~1″-resolution NIR extinction map toward the innermost $\simeq 30'' \times 30''$ region obtained from spectrally-unresolved H_2 observations. They derive an averaged value of $A_{Ks} \simeq 3.4$ and maxima around $A_{Ks} \simeq 4$, thus allowing for local peaks of several magnitudes of visual extinction from dust and gas inside the cavity itself. In particular, some of the

infrared extinction peaks outside the mini-spiral coincide with the position of some ^{12}CO HPVG cloudlets. Therefore, at least qualitatively, the presence of small-scale molecular cloudlets of a few magnitudes of visual extinction inside the cavity, partially shielded from the strong FUV field, does not contradict the existing extinction maps.

O-type massive stars in the central cluster (Becklin & Neugebauer 1968; Krabbe et al. 1995; Schödel et al. 2014, and references therein) produce strong UV radiation fields and launch powerful winds (e.g., Wolfire et al. 1990; Mezger et al. 1996; Genzel et al. 2010). FUV photons heat the interstellar dust to high temperatures, above ~100 K. Hence, MIR and FIR continuum observations of the dust thermal emission (Telesco et al. 1996; Latvakoski et al. 1999; Etxaluze et al. 2011; Lau et al. 2013) can be used to estimate the FUV-photon flux (G_0). The 19.7/31.7 μm color temperature ($T_{\rm col}$) peaks at $T_{\rm d} \approx 145$ K inside the cavity, and is ≈85 K at the inner edge of the CND-S lobe (Lau et al. 2013). We use $G_0 \simeq (T_{\rm d}/12.2)^5$ (see Hollenbach et al. 1991), where we adopt $T_{\rm d}$ (big grains) $\simeq T_{\rm col}$ and assume that the MIR continuum is dominated by the thermal emission of FUV-heated big grains. These color temperatures then imply a FUV flux ranging from $G_{0,\rm Cavity} \approx 10^{5.3}$ to $G_{0,\rm CND} \approx 10^{4.2}$. The assumption that the observed MIR continuum emission is dominated by big grains, and not by stochastically heated very small grains (VSGs) or PAHs out of thermal equilibrium (i.e., Desert et al. 1990), is a reasonable one because the thermal emission peak from hot dust ($T_{\rm d} = 150$–75 K) lies at MIR wavelengths. Hence, this emission will dominate over that of other grain populations. Still, our estimated G_0 values should be considered as upper limits because of the undetermined contribution of VSGs and PAHs to the observed MIR photometric emission (e.g., Berné et al. 2007; Etxaluze et al. 2011, 2013).

Figure 13 shows the location of the HPVG and EPVG molecular cloudlets with respect to the 70 μm dust thermal emission (observed by *Herschel*, Molinari et al. 2011) typically associated with the presence of FUV-irradiated hot/warm neutral material. The 70 μm dust emission is slightly shifted to the east with respect to the ionized gas in the northern arm, as if this streamer (traced by the 6 cm radiocontinuum emission in Fig. 13) was the limb-brightened ionized rim of a roughly edge-on neutral gas structure behind. Several EPVG cloudlets appear distributed along this northern area of bright 70 μm dust emission that also coincides with the so-called northern intruder seen in MIR dust emission (Telesco et al. 1996; Latvakoski et al. 1999), neutral oxygen [O I] 63 μm (Jackson et al. 1993), Br γ (Paumard et al. 2004) and in H_2 line emission (Ciurlo et al. 2016).

Most EPVG cloudlets appear distributed along areas of high 19.7/31.7 μm color temperature ratio (Lau et al. 2013) and bright 70 μm dust emission inside the cavity. If their true location is not very different from the dust-emitting regions, the molecular cloudlets are certainly irradiated by strong FUV-radiation fields (Wolfire et al. 1990) and heated, predominantly by shocks, to temperatures of several hundred K (e.g., Goicoechea et al. 2013, 2018; Mills et al. 2017). The HPVG cloudlets, are distributed along areas of weaker 70 μm dust emission, representative of lower FUV-irradiation conditions or lower column densities of neutral material.

The attenuation of the FUV-field from the central cavity to the inner edge of the CND-S lobe implies a dust column density equivalent to $A_V \approx 1$–2 mag of local visual extinction, where

$$A_V \approx -(1/\kappa_{\rm FUV})/(\tau_{\rm FUV}/\tau_V)\ \ln(G_{0,\rm CND}/G_{0,\rm Cavity}). \quad (6)$$

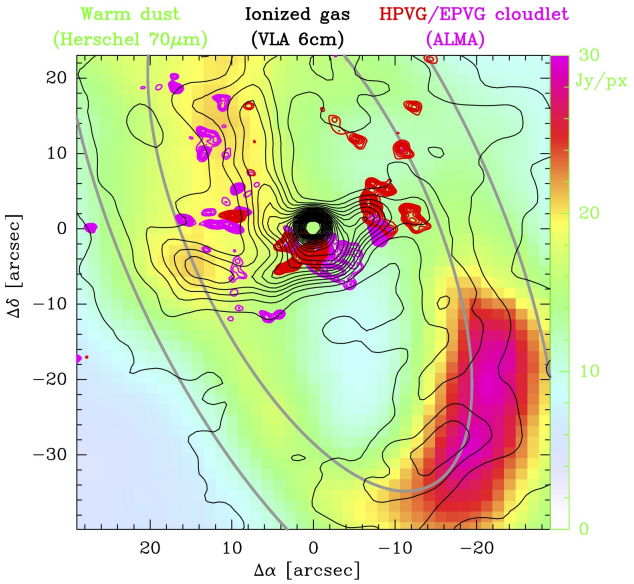

Fig. 13. Location of the HPVG (red) and EPVG (magenta) ^{12}CO cloudlets detected by ALMA over a color image of the warm (FUV-irradiated) dust emission taken by *Herschel*/PACS at 70 μm. Black contours show the ionized gas streamers observed by VLA in 6 cm radio-continuum emission (Yusef-Zadeh & Morris 1987).

In the above relation, $\tau_{\rm FUV}/\tau_V$ is the extinction curve at FUV wavelengths and the $\kappa_{\rm FUV}$ parameter (≈1) depends on grain properties (Goicoechea & Le Bourlot 2007) and metallicity (Mezger et al. 1996). Hence, the approximate extinction values derived from Eq. (6) are consistent with the average values estimated from the ^{12}CO cloudlet emission in the previous section.

Taking a representative FUV photon flux of $G_0 = 10^{4.7}$ and using updated ^{12}CO photodissociation rates (Visser et al. 2009), we derive that the photodissociation timescale ($\tau_{\rm ph}$) of cloudlets within the cavity will be short: $\approx 10^5$, 2×10^4, and a few hundred years for cloudlets with visual extinction peaks $A_V = 5$, 4, and 3 mag respectively. In addition, we derive the extinction that would allow the molecular gas in the inner edge of the CND to perform one complete turn before being photodissociated. The A_V satisfying $\tau_{\rm rot}(\varphi) = \tau_{\rm ph}(^{12}{\rm CO})$ for $G_{0,\rm CND} = 10^{4.2}$ amounts to $A_V \approx 4$ mag of visual extinction. This value argues in favor of rather low column densities of material at the inner CND-S edge, and thus consistent with the relatively modest inferred masses.

4.5. Absorption spectrum: foreground diffuse gas

Sgr A* is a strong synchrotron submillimeter emitter, with a continuum emission that peaks around 350 GHz (Marrone et al. 2006; Eckart et al. 2012; Moser et al. 2017). For a given continuum equivalent brightness temperature $T_{\rm c}$, any foreground molecular gas component in the line-of-sight will be observed in absorption if $T_{\rm rot} < T_{\rm c}$. The central continuum source has a compact size, thus a pencil-beam spectrum toward Sgr A* can reveal these components.

Because CO is the most abundant molecule after H_2, CO absorption measurements are a very convenient probe of small column densities of low excitation molecular gas, that is, low $T_{\rm rot}$ but not necessarily low $T_{\rm k}$ if gas densities are very low and $T_{\rm c}$ is high. Figure 14 shows the 1″-resolution ^{12}CO ($J = 3$–2) spectrum taken with the ALMA interferometer alone, no zero-spacing data added, toward Sgr A* (black histogram). Many ^{12}CO spectral features are detected in absorption. This

spectrum provides a radiography of the low excitation gas in the line-of-sight toward the Galactic center and of diffuse gas potentially close to Sgr A* (see Table 1 for the parameters obtained for each feature). SO and $H^{13}CN$ are much less abundant than CO, in other words, much lower columns of absorbing material, and their rotationally excited levels are more difficult to populate in low density gas. This explains the lack of SO 8_9–7_8 and $H^{13}CN$ $J = 4$–3 line absorption toward the continuum emission of Sgr A*.

Figure 14 also shows the ^{12}CO ($J = 3$–2) spectrum (green) averaged over the entire ALMA field, and adding the zero-spacing data. This other spectrum is dominated by CO emission from the Galactic center. Comparing both spectra allows one to better understand the velocity components that more certainly arise from gas close to Sgr A* in the ALMA images.

The velocity range $|v_{LSR}| < 100$ km s^{-1} has been widely studied in absorption measurements[3]. It includes absorptions produced by low-density molecular clouds in the spiral arms of the Galaxy: the 3-kpc arm, 4-kpc arm, Sagittarius, and Scutum arms, and by clouds in the Galactic center region (Greaves & Williams 1994; Sandqvist et al. 2015). The ALMA spectrum also shows an absorption feature at $v_{LSR} \simeq -73$ km s^{-1} that is not present in single-dish, low angular resolution, absorption spectra (see e.g. in H_2O ground-state line measurements, Sandqvist et al. 2003). The feature has a considerable absorption depth, $\tau_{abs,CO\,3-2} \simeq -\ln(T/T_c) \simeq 0.8$, equivalent to $N(CO) \approx 2 \times 10^{17}$ cm^{-2} (or $N(H_2) \approx 5 \times 10^{21}$ cm^{-2}) for the absorbing material (see below). VLA observations show an OH absorption feature at $v_{LSR} \simeq -73$ km s^{-1} as well, but only toward the CND-S lobe (Karlsson et al. 2015). The fact that we detect it toward Sgr A* implies that it is more extended around the CND. Table 1 shows our estimated column densities of absorbing CO calculated by integrating each velocity component:

$$N_{abs}(CO) \approx 4.81 \times 10^{16} \int \tau_{abs,CO\,3-2}(v)\,dv, \quad (7)$$

where we have assumed $T_{rot} = 5$ K. To derive the equivalent $N(H_2)$ columns we use $N(CO)/N(H_2) = 4 \times 10^{-5}$ (see discussion in Sect. 4.3). These column densities would be a factor ~2 higher if one assumes a more elevated T_{rot}=10 K.

As expected, the ^{12}CO spectrum shows a deep absorption feature at $v_{LSR} \simeq -135$ km s^{-1} produced by foreground gas that follows, driven by the barred potential of the Galaxy, non-circular x_1 orbits around the Galactic center and produces the characteristic parallelogram on (l, v) longitud-velocity CO maps (e.g., Bally et al. 1988; Binney et al. 1991). This component was first interpreted, and is still often referred to, as an expanding molecular ring (Scoville 1972; Liszt & Burton 1978). The observed weaker absorptions at $v_{LSR} \simeq -121$ and -145 km s^{-1} are likely part of the same widespread structure, that is, molecular gas located in the inner few hundred parsecs

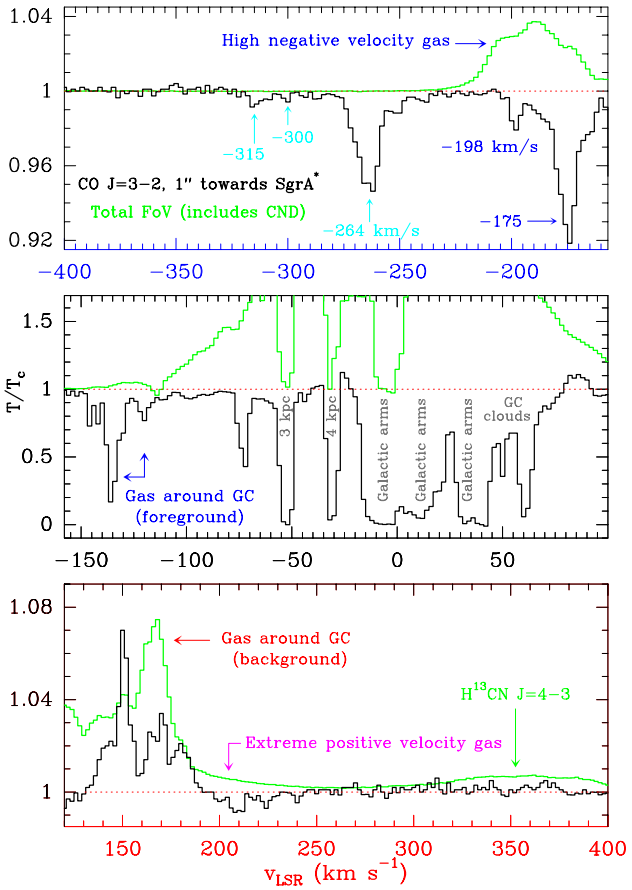

Fig. 14. ^{12}CO ($J = 3$–2) spectrum toward Sgr A*. The three panels cover the LSR velocity range from −400 to +400 km s^{-1}. The black histogram (dominated by line absorption) is the 1″-angular resolution spectrum toward the bright continuum source at Sgr A*. The green histogram (dominated by line emission) is the average spectrum over the ≃60″ × 60″ field-of-view observed by ALMA.

of the Galaxy but not associated with the Sgr A complex. In addition, there are features at more negative velocities. Some of these absorptions, those at $v_{LSR} \simeq -175$ and -198 km s^{-1}, coincide with the so-called -180 km s^{-1} feature (Guesten & Downes 1981; Liszt & Burton 1993). This absorption component arises from HNVG clouds, most likely a massive cloud falling toward the Galactic center area (Zhao et al. 1995). Coincidence or not, the -180 km s^{-1} velocity channel map in Fig. 4 shows that the emission counterpart resembles a stretched cloud distorted by a central gravitational force (see model by Zhao et al. 1995). Marshall & Lasenby (1994) detected, in low resolution single-dish observations, extended ^{12}CO $J = 3$–2 and 2-1 line emission at these negative velocities. From the measured low 3–2/2–1 line intensity ratio they estimated cold rotational temperatures, $T_{rot} = 8$–10 K $\lesssim T_k$, typical of quiescent cold clouds not heated by FUV photons from nearby massive stars. They associate the HNVG component to the large-scale galactic gas distribution and not with the environment around Sgr A*. In the ALMA images, this velocity range shows many filamentary structures through the field (Fig. 4). Hence, owing to foreground structures at $v_{LSR} \simeq -200$ to -150 km s^{-1}, one cannot easily associate the cloudlets detected in this negative range with Sgr A* surroundings.

Surprisingly, the ^{12}CO absorption spectrum in Fig. 14 shows two additional weak features at more extreme negative-velocities ($v_{LSR} = -264$ and -310 km s^{-1}) that have not been reported

[3] We checked that no line from a molecule different than CO could be responsible of the observed spectral features. Only the absorption feature at -121 ± 2 km s^{-1} may be blended with the SH^+ 1_0–0_1 $F = 1/2$–$3/2$ line at 345.944 GHz (Müller et al. 2014) if the intrinsic SH^+ absorption toward Sgr A* peaks at $v_{LSR} \simeq +7$ km s^{-1}. The weaker SH^+ fine structure component F=1/2–1/2 at 345.858 GHz would then be the small absorption peak at ≃−46 km s^{-1}. Although SH^+ absorption lines are known to exist toward the Galactic center (e.g., Godard et al. 2012) and even if the CO absorption peak at -121 ± 2 km s^{-1} is blended, we don't expect detectable SH^+ emission in the ALMA images; for example in the Orion Bar, the ^{12}CO ($J = 3$–2) line is >500 times brighter that the SH^+ 1_0–0_1 $F = 1/2$–$3/2$ line (Goicoechea et al. 2017).

Table 1. CO ($J = 3$–2) line absorption velocity components toward Sgr A* continuum source and estimated column densities.

v_{LSR}[a] (km s^{-1})	Width[a], Δv (km s^{-1})	Depth, $\tau_{abs,CO\,3-2}$	N_{abs}(CO)[b] (cm^{-2})	$N(H_2)$[c] (cm^{-2})	Component[d]
-315 ± 3	3 ± 1	0.009	1.27×10^{15}	3.17×10^{19}	*New*. ENVG. Near Sgr A*?
-264 ± 1	11 ± 1	0.053	2.89×10^{16}	7.23×10^{20}	*New*. ENVG. Near Sgr A*?
-198 ± 1	5 ± 3	0.021	4.83×10^{15}	1.21×10^{20}	HNVG. Foreground cloud
-175 ± 1	11 ± 1	0.086	4.76×10^{16}	1.19×10^{21}	HNVG. Foreground cloud
-145 ± 2	4 ± 1	0.269	4.91×10^{16}	1.23×10^{21}	Foreground gas around GC?
-135 ± 2	7 ± 2	1.309	4.33×10^{17}	1.08×10^{22}	Foreground gas around GC
-121 ± 2	6 ± 2	0.269	8.48×10^{16}	2.12×10^{21}	Foreground gas around GC?
-73 ± 1	5 ± 1	0.842	2.09×10^{17}	5.22×10^{21}	CND?
-53 ± 1	6 ± 1	$\gg 1$	–	–	3-kpc arm feature
-31 ± 1	5 ± 1	$\gg 1$	–	–	-30 km s^{-1} or 4-kpc arm
-7 ± 1	19 ± 1	$\gg 1$	–	–	Galactic arms
12 ± 1	16 ± 1	$\gg 1$	–	–	Galactic arms
37 ± 1	21 ± 1	$\gg 1$	–	–	GC clouds
50 ± 1	5 ± 1	0.734	1.76×10^{17}	4.41×10^{21}	GC clouds
61 ± 1	8 ± 1	2.523	1.01×10^{18}	2.54×10^{22}	GC clouds

Notes. [a]From a multigaussian fit to the 1″-resolution spectrum toward Sgr A*. [b]Assuming $T_{rot}(CO) = 5$ K. [c]Assuming $N(CO)/N(H_2) = 4 \times 10^{-5}$. [d]ENVG = extreme negative velocity gas, HNVG = high negative velocity gas, GC = Galactic center, CND = circumnuclear disk.

before (e.g., Zhao et al. 1995; Sandqvist et al. 2003; Godard et al. 2012). We term these absorption features at $v_{LSR} < -250$ km s^{-1} the *extreme negative-velocity gas* (ENVG) component. These velocities do not show emission counterpart in the ALMA images either. One interpretation is that they are produced by low density diffuse molecular gas in front of and close to Sgr A*. Given the enclosed mass model and expected velocities, we estimate that they would be located at about 0.04–0.1 pc (50–120 light-day) if they follow trajectories with the same inclination as the CND.

The background molecular gas following x_1 orbits around the Galactic center, that is, the positive-velocity side of the (l, v) parallelogram, is expected to be seen in CO emission (at $v_{LSR} \simeq +150$–165 km s^{-1}) because it is located behind the continuum source at Sgr A* (Binney et al. 1991). The ALMA images (Fig. 4) show both an extended emission, likely dominated by emission from this background component, and several clumpy features that we attribute to gas closer to Sgr A*.

Finally, the ^{12}CO spectrum averaged over the field shows an emission wing up to $v_{LSR} \simeq +300$ km s^{-1}. This wing is also detected in deep single-dish observations of rotationally excited mid-J CO lines toward Sgr A* (Goicoechea et al. 2018). At these extreme velocities, the ALMA images unveil a collection of ^{12}CO EPVG cloudlets.

5. Discussion

5.1. Most cloudlets inside the cavity do not fit the kinematics of the ionized gas streamers

In addition to the small spatial-scale molecular emission resolved toward the central cavity, perhaps the most relevant result of this work is that the bulk of high and extreme positive-velocity ^{12}CO cloudlets ($v_{LSR} \approx +150$ to $+300$ km s^{-1}) do not fit any of the kinematical models proposed for the ionized gas motions: spirals from the CND or ellipses around Sgr A*. Only the molecular structures A and B (cloudlet #1) appear at the predicted positions and velocities of the Keplerian ellipse model. Instead, most HPVG and EPVG cloudlets are distributed over a relatively extended area of the cavity (radius <15″ or 0.6 pc) and all show similarly high velocities and broad line-widths ($\Delta v \simeq 25$–40 km s^{-1}, see Table B.1). Their line profiles are not doubled-peaked, so they do not seem consistent with the expected emission from gas in rotating protoplanetary disks (e.g., Dutrey et al. 1997) or from photoevaportaing disks (proplyds), as previously suggested for other features toward the cavity (e.g., Yusef-Zadeh et al. 2015).

Their similar line centroid velocity and broad line-widths, as well as lack of associated bright ionized gas emission counterpart are puzzling. They may be compatible with the debris of a tidally disrupted molecular cloud or clump that fell into the region. The higher molecular gas velocities would imply a particularly fast molecular cloud, perhaps two, one for the HPVG and another one for the EPVG cloudlets, that fell from larger distances (Oka et al. 2011; Hsieh et al. 2017) not so long ago; owing to the fast photo-evaporation timescales, got tidally disrupted in the cavity, and the densest leftovers are now resolved by ALMA as cloudlets. However, no physical process has been identified yet for scattering clouds onto orbits that have a low phase-space probability likelihood. Alternatively, the presence of molecular cloudlets inside the cavity might be accounted for instabilities in the inner rim of the CND that lead to fragmentation and infall from there (e.g., Blank et al. 2016), through orbits that we have not modeled here. Such process may also allow faster replenishment of the molecular gas in the cavity.

In addition, dissipative effects such as shocks in colliding streams, cloudlet-cloudlet collisions, and colliding stellar winds (e.g., Calderón et al. 2016), or UV-induced dynamical effects produced by advancing photoionization fronts (e.g., Goicoechea et al. 2016), may trigger enough gas compression and molecular gas formation. This may provide an explanation for structures A and B. Higher resolution observations of their proper motions are obviously needed to clarify their origin and fate.

5.2. Molecular gas reservoir inside the cavity

From the CO ($J = 3$–2) images we have estimated the mass of the EPVG component inside the central cavity: ~6–12 $M_\odot$ (range $+200 < v_{LSR} < +300$ km s^{-1}) plus ≤45–190 $M_\odot$ in the

HPVG range ($+150 < v_{\rm LSR} < +200$ km s^{-1}). The low-J CO emission from the latter velocity range, however, is affected by lower-excitation CO extended emission from the background, not related to Sgr A* surroundings. Recent detection of high positive-velocity emission wings in more excited CO rotational lines (up to $J = 10$–9) provides further evidence that molecular gas inside the cavity exists and is hot; contribution to the mid-J CO emission from the background is likely negligible (Goicoechea et al. 2018). These authors estimated a mass of ~10–60 $M_\odot$ for this hot molecular gas component.

Overall, the inferred molecular mass inside the cavity is low, but much higher than that previously estimated from infrared H_2 line observations (<0.5 $M_\odot$, Ciurlo et al. 2016; Mills et al. 2017). Our derived molecular gas mass is in the order, or slightly below, of the estimated neutral atomic gas mass (~50–300 $M_\odot$, Jackson et al. 1993; Telesco et al. 1996; Latvakoski et al. 1999) and higher than the ~60 $M_\odot$ inferred in the ionized gas streamers (e.g., Lo & Claussen 1983; Jackson et al. 1993; Irons et al. 2012). As any dense photo-dissociation region (PDR) close to massive stars (e.g., Hollenbach & Tielens 1997; Goicoechea et al. 2016), these different masses suggest that the cloudlets have a stratified PDR structure (onion-like): with the infrared H_2 emission arising from the outermost and more FUV-irradiated layers, and the low-J ^{12}CO emission tracing the bulk of cloudlet mass. According to the low estimated masses, the cloudlets are not massive enough, individually, to be gravitationally bound ($M_{\rm Cloudlet} \ll M_{\rm Virial}$) so that it is unlikely that they will form new stars unless much material is accumulated, but see alternative scenarios in Yusef-Zadeh et al. (2017b). Given the rapid photo-evaporation timescales, this process would have to be quick enough to replenish this molecular gas reservoir in such a harsh, dynamic, and strong gravity environment.

Using the inferred HPVG and EPVG cloudlet masses and adopting representative velocities of 150 and 250 km s^{-1} for their motion, we estimate infall rates of 10^{-2} and 10^{-3} $M_\odot$ yr^{-1} respectively. This means that the detected cloudlets inside the cavity are fresh molecular material that has accumulated only in the last $\lesssim 10^4$ yr. This is consistent with the photo-dissociation timescales of cloudlets with $A_{\rm V} \lesssim 4$ mag. Hence, the detected extended and diffuse ($A_{\rm V} \lesssim 0.5$ mag) molecular gas component has to be a very short-lived component: continuously replenished by cloudlets' photo-evaporation and tidal disruption.

6. Summary and conclusions

The Galactic center is about 100 times closer than any active galactic nucleus. Hence, it offers a unique laboratory to study in exquisite detail the evolution of interstellar gas and massive stars in the strong gravitational potential of a SMBH and nuclear stellar cluster. We have presented new images of the molecular gas emission toward the central parsec of the Milky Way obtained with ALMA at 1″ angular resolution (~0.04 pc). Our results include the first unambiguous detection high velocity molecular cloudlets inside the cavity of the CND.

The ALMA images show that the southern lobe of the CND has a clumpy gas distribution, as traced by H^{13}CN $J = 4$–3 and SO 8_9–7_8 lines. Its motion requires a bundle of nonuniformly rotating streamers of slightly different inclinations. The inferred gas density peaks, molecular cores of several 10^5 cm^{-3}, are much lower than the local Roche density, so we agree with previous works that the CND cores are transient (Mills et al. 2013; Smith & Wardle 2014), in other words, they will be stretched and disrupted instead of forming gravitationally bound prestellar cores. However, hydrodynamical simulations show that this conclusion does not immediately imply that the entire CND is a transient entity. Instabilities within the CND, or in the interaction layer between the outflowing winds from massive stars and the inner edge of the CND, can generate transient structures within a relatively stable CND (e.g., Blank et al. 2016).

Inside the cavity and in the inner rim of the CND, the molecular gas is irradiated by a strong FUV field produced by massive stars in the central cluster. We estimate $G_{0,\rm Cavity} \simeq 10^{5.3}$ and $G_{0,\rm CND} \simeq 10^{4.3}$ respectively. The required attenuation of the FUV radiation flux implies $A_V \simeq 1$–2 mag of local visual extinction within the cavity, that is, it is not devoid of insterstellar gas and dust. In particular, the detection of small spatial-scale ^{12}CO gas structures close to Sgr A*, and moving at high velocities, confirms that the central cavity is not fully cleared of molecular gas. It rather accepts a small fraction, at rates of 10^{-2}–10^{-3} $M_\odot$ yr^{-1}, that falls from the inner rim of the CND or from molecular clouds that plunge from larger distances. In either case, molecular cloudlets entering the cavity will be unstable against tidal shear from the SMBH. We have likely detected the products of this tidal fragmentation: the densest fragments, the cloudlets, and a lower density and short-lived extended component. Evidence for such diffuse intercloudlet gas is suggested by the ^{12}CO images and also by the absorption spectrum toward Sgr A* synchrotron emission.

Except for two intriguing structures (A and B in Figs. 5 and 11) we conclude that the velocities of the detected cloudlets do not match those of the ionized streamers orbits. Instead, molecular cloudlets show similar velocity centroids and broad-line profiles over a relatively large area of the cavity. This may suggest that they were part of a more massive molecular cloud or clump, perhaps two, that fell to the inner region and got disrupted $\lesssim 10^4$ yr ago. Yet, no process has been identified for scattering clouds onto such inner impact parameter orbits. Alternatively, the observed cloudlets may originate from instabilities in the inner rim of the CND that lead to fragmentation and infall from there.

It remains unclear whether this molecular gas reservoir inside the cavity would ever grow enough to form a new generation of stars or if it would be photo-evaporated and ionized by the strong stellar UV field in the region, completely disrupted by the strong gravitational tidal shears, or blown away by stellar winds from the central cluster. While it is unlikely that the observed cloudlets will directly form new massive stars, their presence is a piece of the puzzle toward understanding the formation of stars close to SMBHs, the stability of CNDs, and the influence of nuclear stellar clusters.

Acknowledgements. We thank our referee Mark Morris for useful comments and suggestions. We thank the ERC for support under grant ERC-2013-Syg-610256-NANOCOSMOS. We also thank Spanish MCIU for funding supports under grant AYA2017-85111-P. JP and MG acknowledge by the Programme National Physique et Chimie du Milieu Interstellaire (PCMI) of CNRS/INSU with INC/INP co-funded by CEA and CNES. ALMA is a partnership of ESO (representing its member states), NSF (USA) and NINS (Japan), together with NRC (Canada), NSC and ASIAA (Taiwan), and KASI (Republic of Korea), in cooperation with the Republic of Chile. The Joint ALMA Observatory is operated by ESO, AUI/NRAO, and NAOJ.

References

Baganoff, F. K., Maeda, Y., Morris, M., et al. 2003, ApJ, 591, 891
Bally, J., Stark, A. A., Wilson, R. W., & Henkel, C. 1988, ApJ, 324, 223
Becklin, E. E., & Neugebauer, G. 1968, ApJ, 151, 145
Becklin, E. E., Gatley, I., & Werner, M. W. 1982, ApJ, 258, 135
Berné, O., Joblin, C., Deville, Y., et al. 2007, A&A, 469, 575
Binney, J., Gerhard, O. E., Stark, A. A., Bally, J., & Uchida, K. I. 1991, MNRAS, 252, 210

Blank, M., Morris, M. R., Frank, A., Carroll-Nellenback, J. J., & Duschl, W. J. 2016, MNRAS, 459, 1721
Boger, G. I., & Sternberg, A. 2005, ApJ, 632, 302
Bolatto, A. D., Wolfire, M., & Leroy, A. K. 2013, ARA&A, 51, 207
Calderón, D., Ballone, A., Cuadra, J., et al. 2016, MNRAS, 455, 4388
Cernicharo, J., & Guelin, M. 1987, A&A, 176, 299
Christopher, M. H., Scoville, N. Z., Stolovy, S. R., & Yun, M. S. 2005, ApJ, 622, 346
Cicone, C., Maiolino, R., Sturm, E., et al. 2014, A&A, 562, A21
Ciurlo, A., Paumard, T., Rouan, D., & Clénet, Y. 2016, A&A, 594, A113
Desert, F.-X., Boulanger, F., & Puget, J. L. 1990, A&A, 237, 215
Dutrey, A., Guilloteau, S., & Guelin, M. 1997, A&A, 317, L55
Eckart, A., García-Marín, M., Vogel, S. N., et al. 2012, A&A, 537, A52
Etxaluze, M., Smith, H. A., Tolls, V., Stark, A. A., & González-Alfonso, E. 2011, AJ, 142, 134
Etxaluze, M., Goicoechea, J. R., Cernicharo, J., et al. 2013, A&A, 556, A137
Feldmeier-Krause, A., Neumayer, N., Schödel, R., et al. 2015, A&A, 584, A2
Ferrière, K. 2012, A&A, 540, A50
García-Burillo, S., Combes, F., Usero, A., et al. 2014, A&A, 567, A125
Geballe, T. R., Wade, R., Krisciunas, K., Gatley, I., & Bird, M. C. 1987, ApJ, 320, 562
Genzel, R., Lutz, D., Sturm, E., et al. 1998, ApJ, 498, 579
Genzel, R., Eisenhauer, F., & Gillessen, S. 2010, Rev. Mod. Phys., 82, 3121
Ghez, A. M., Salim, S., Weinberg, N. N., et al. 2008, ApJ, 689, 1044
Gillessen, S., Eisenhauer, F., Trippe, S., et al. 2009, ApJ, 692, 1075
Gillessen, S., Genzel, R., Fritz, T. K., et al. 2012, Nature, 481, 51
Godard, B., Falgarone, E., Gerin, M., et al. 2012, A&A, 540, A87
Goicoechea, J. R., & Le Bourlot, J. 2007, A&A, 467, 1
Goicoechea, J. R., Pety, J., Gerin, M., et al. 2006, A&A, 456, 565
Goicoechea, J. R., Etxaluze, M., Cernicharo, J., et al. 2013, ApJ, 769, L13
Goicoechea, J. R., Pety, J., Cuadrado, S., et al. 2016, Nature, 537, 207
Goicoechea, J. R., Cuadrado, S., Pety, J., et al. 2017, A&A, 601, L9
Goicoechea, J. R., Santa-Maria, M. G., Teyssier, D., et al. 2018, A&A, 616, L1
Gonzalez-Alfonso, E., & Cernicharo, J. 1993, A&A, 279, 506
Goto, M., Geballe, T. R., Indriolo, N., et al. 2014, ApJ, 786, 96
Greaves, J. S., & Williams, P. G. 1994, A&A, 290, 259
Guesten, R., & Downes, D. 1981, A&A, 99, 27
Guesten, R., Genzel, R., Wright, M. C. H., et al. 1987, ApJ, 318, 124
Herrnstein, R. M., & Ho, P. T. P. 2002, ApJ, 579, L83
Hollenbach, D. J., & Tielens, A. G. G. M. 1997, ARA&A, 35, 179
Hollenbach, D. J., Takahashi, T., & Tielens, A. G. G. M. 1991, ApJ, 377, 192
Hsieh, P.-Y., Koch, P. M., Ho, P. T. P., et al. 2017, ApJ, 847, 3
Irons, W. T., Lacy, J. H., & Richter, M. J. 2012, ApJ, 755, 90
Jackson, J. M., Geis, N., Genzel, R., et al. 1993, ApJ, 402, 173
Joblin, C., Bron, E., Pinto, C., et al. 2018, A&A, 615, A129
Karlsson, R., Sandqvist, A., Fathi, K., & Martín, S. 2015, A&A, 582, A118
Krabbe, A., Genzel, R., Eckart, A., et al. 1995, ApJ, 447, L95
Lacy, J. H., Townes, C. H., Geballe, T. R., & Hollenbach, D. J. 1980, ApJ, 241, 132
Lacy, J. H., Achtermann, J. M., & Serabyn, E. 1991, ApJ, 380, L71
Latvakoski, H. M., Stacey, G. J., Gull, G. E., & Hayward, T. L. 1999, ApJ, 511, 761
Lau, R. M., Herter, T. L., Morris, M. R., Becklin, E. E., & Adams, J. D. 2013, ApJ, 775, 37
Liszt, H. S. 2003, A&A, 408, 1009
Liszt, H. S., & Burton, W. B. 1978, ApJ, 226, 790
Liszt, H. S., & Burton, W. B. 1993, ApJ, 407, L25
Lo, K. Y., & Claussen, M. J. 1983, Nature, 306, 647
Marrone, D. P., Moran, J. M., Zhao, J.-H., & Rao, R. 2006, ApJ, 640, 308
Marrone, D. P., Moran, J. M., Zhao, J.-H., & Rao, R. 2007, ApJ, 654, L57
Marshall, J., & Lasenby, A. N. 1994, MNRAS, 269, 619
Martín, S., Martín-Pintado, J., Montero-Castaño, M., Ho, P. T. P., & Blundell, R. 2012, A&A, 539, A29
Mezger, P. G., Duschl, W. J., & Zylka, R. 1996, A&ARv, 7, 289
Mills, E. A. C., Güsten, R., Requena-Torres, M. A., & Morris, M. R. 2013, ApJ, 779, 47
Mills, E. A. C., Togi, A., & Kaufman, M. 2017, ApJ, 850, 192
Molinari, S., Bally, J., Noriega-Crespo, A., et al. 2011, ApJ, 735, L33
Moneti, A., Cernicharo, J., & Pardo, J. R. 2001, ApJ, 549, L203
Montero-Castaño, M., Herrnstein, R. M., & Ho, P. T. P. 2009, ApJ, 695, 1477
Morris, M., & Serabyn, E. 1996, ARA&A, 34, 645
Moser, L., Sánchez-Monge, Á., Eckart, A., et al. 2017, A&A, 603, A68
Moultaka, J., Eckart, A., & Mužić, K. 2015, ApJ, 806, 202
Müller, H. S. P., Goicoechea, J. R., Cernicharo, J., et al. 2014, A&A, 569, L5
Oka, T., Nagai, M., Kamegai, K., & Tanaka, K. 2011, ApJ, 732, 120
Paumard, T., Maillard, J.-P., & Morris, M. 2004, A&A, 426, 81
Pety, J., & Rodríguez-Fernández, N. 2010, A&A, 517, A12
Requena-Torres, M. A., Güsten, R., Weiß, A., et al. 2012, A&A, 542, L21
Roberts, D. A., Yusef-Zadeh, F., & Goss, W. M. 1996, ApJ, 459, 627
Rogstad, D. H., Lockhart, I. A., & Wright, M. C. H. 1974, ApJ, 193, 309
Sandqvist, A., Bergman, P., Black, J. H., et al. 2003, A&A, 402, L63
Sandqvist, A., Larsson, B., Hjalmarson, Å., et al. 2015, A&A, 584, A118
Schödel, R., Ott, T., Genzel, R., et al. 2002, Nature, 419, 694
Schödel, R., Eckart, A., Alexander, T., et al. 2007, A&A, 469, 125
Schödel, R., Najarro, F., Muzic, K., & Eckart, A. 2010, A&A, 511, A18
Schödel, R., Feldmeier, A., Kunneriath, D., et al. 2014, A&A, 566, A47
Scoville, N. Z. 1972, ApJ, 175, L127
Serabyn, E., & Lacy, J. H. 1985, ApJ, 293, 445
Smith, I. L., & Wardle, M. 2014, MNRAS, 437, 3159
Telesco, C. M., Davidson, J. A., & Werner, M. W. 1996, ApJ, 456, 541
Trani, A. A., Mapelli, M., & Ballone, A. 2018, ApJ, 864, 17
Tsuboi, M., Kitamura, Y., Uehara, K., et al. 2018, PASJ, in press [arXiv:1806.10246]
Visser, R., van Dishoeck, E. F., & Black, J. H. 2009, A&A, 503, 323
Wolfire, M. G., Tielens, A. G. G. M., & Hollenbach, D. 1990, ApJ, 358, 116
Yusef-Zadeh, F., & Morris, M. 1987, ApJ, 320, 545
Yusef-Zadeh, F., Stolovy, S. R., Burton, M., Wardle, M., & Ashley, M. C. B. 2001, ApJ, 560, 749
Yusef-Zadeh, F., Royster, M., Wardle, M., et al. 2013, ApJ, 767, L32
Yusef-Zadeh, F., Roberts, D. A., Wardle, M., et al. 2015, ApJ, 801, L26
Yusef-Zadeh, F., Cotton, B., Wardle, M., et al. 2017a, MNRAS, 467, 922
Yusef-Zadeh, F., Wardle, M., Kunneriath, D., et al. 2017b, ApJ, 850, L30
Zhao, J.-H., Goss, W. M., & Ho, P. T. P. 1995, ApJ, 450, 122
Zhao, J.-H., Morris, M. R., Goss, W. M., & An, T. 2009, ApJ, 699, 186
Zhao, J.-H., Blundell, R., Moran, J. M., et al. 2010, ApJ, 723, 1097

Appendix A: ALMA images with and without total power single-dish maps

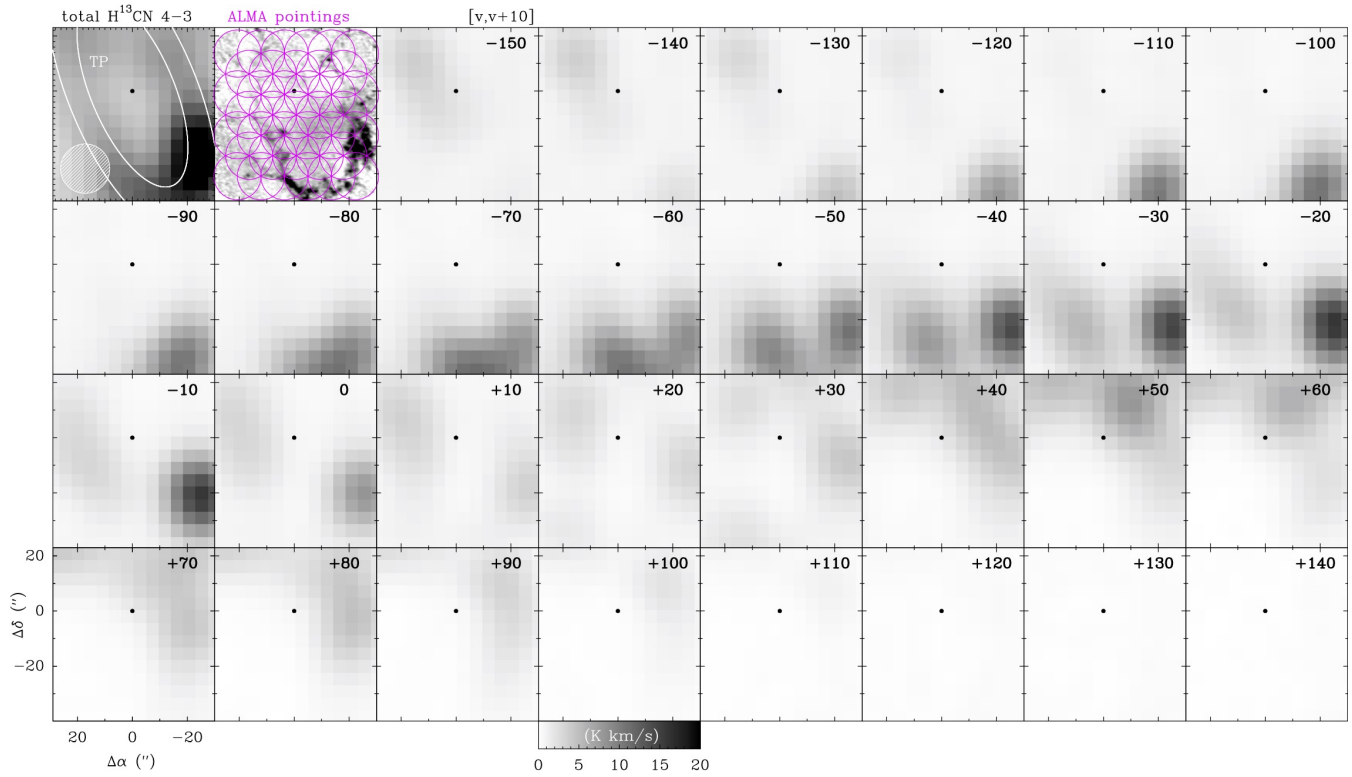

Fig. A.1. Total power (single-dish) $H^{13}CN$ ($J = 4$–3) channel map observations at ∼18″ angular resolution used as zero-spacings. The beam FWHM is shown by the hatched circle. The second panel shows the merged ALMA+zero-spacing data as well as the ALMA interferometer array pointings.

Figure A.1 shows the deep total-power (TP) map obtained for $H^{13}CN$ ($J = 4$–3) and merged with the ALMA array visibilities to produce the final ALMA+TP images shown in the paper. Figures A.2 and A.3 show ^{12}CO ($J = 3$–2), $H^{13}CN$ ($J = 4$–3) line velocity channel maps obtained from ALMA interferometric data alone, without zero-spacing. The images show the intrinsically small spatial scale molecular emission (HPVG and EPVG cloudlets). Figures A.4 and A.5 show the final channel maps after adding the zero-spacing data (single-dish maps) and revealing a more extended emission filtered-out by the ALMA array-only data.

Figures A.2 and A.4 demonstrate the nearly identical spatial distribution of the $H^{13}CN$ ($J = 4$–3) and SO 8_9–7_8 emission. The bright cloudlets appearing at negative velocities with respect to the $H^{13}CN$ $J = 4$–3 line frequency (black images), but absent in the SO (8_9–7_8) images (magenta contours), are not produced by $H^{13}CN$ but by extreme positive ^{12}CO ($J = 3$–2) emission features.

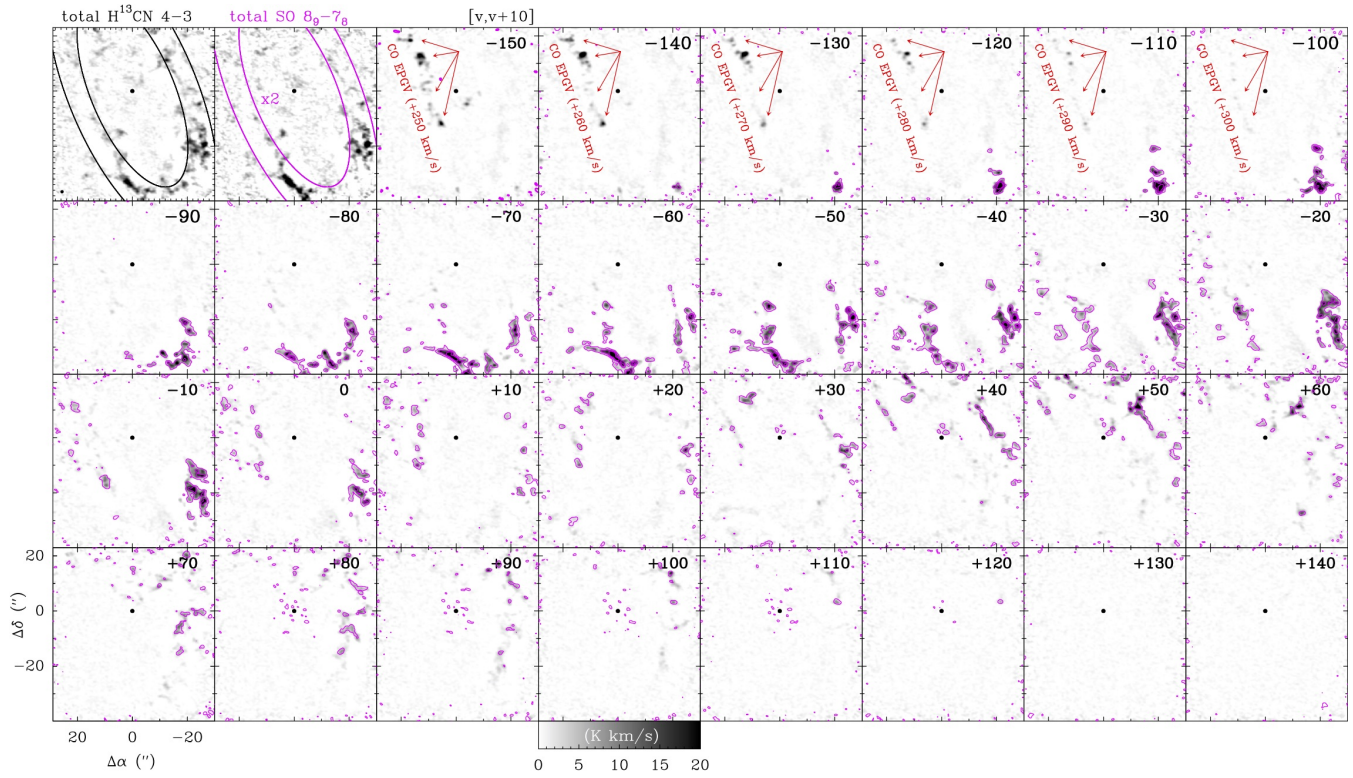

Fig. A.2. Nearly identical spatial distribution of $H^{13}CN$ ($J=4$–3) and SO (8_9–7_8) from ALMA interferometer data alone (zero-spacing data not merged). The *two top left panels* show total integrated line intensity maps. The other maps show $H^{13}CN$ ($J=4$–3) (black images) and SO (8_9–7_8) (magenta contours) channel maps from v_{LSR}=−150 to +150 km s^{-1} in steps of 10 km s^{-1}. At all velocities, most $H^{13}CN$ and SO features spatially match (i.e., they belong to the same gas structure). The emission features seen at negative velocities without SO emission counterpart, however, do not arise from blue-shifted $H^{13}CN$ emission but from red-shifted ^{12}CO cloudlets. Sgr A* is at position (0″, 0″).

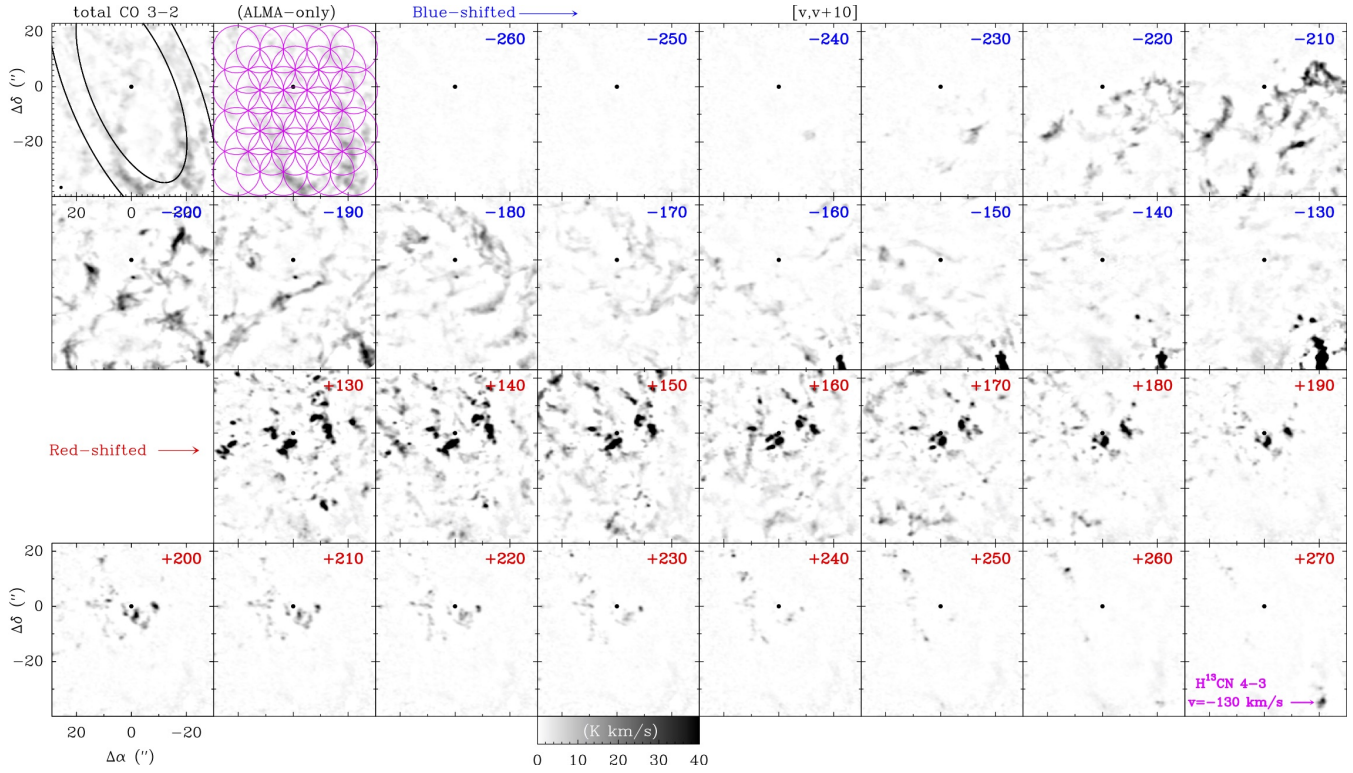

Fig. A.3. ALMA (interferometer only, not including zero-spacing data) ^{12}CO ($J=3$–2) channel emission maps from v_{LSR} = −260 to −120 km s^{-1} (blue-shifted) and from v_{LSR} = +130 to +280 km s^{-1} (red-shifted) in steps of 10 km s^{-1}. Sgr A*, at position (0″, 0″), is displayed with a black dot.

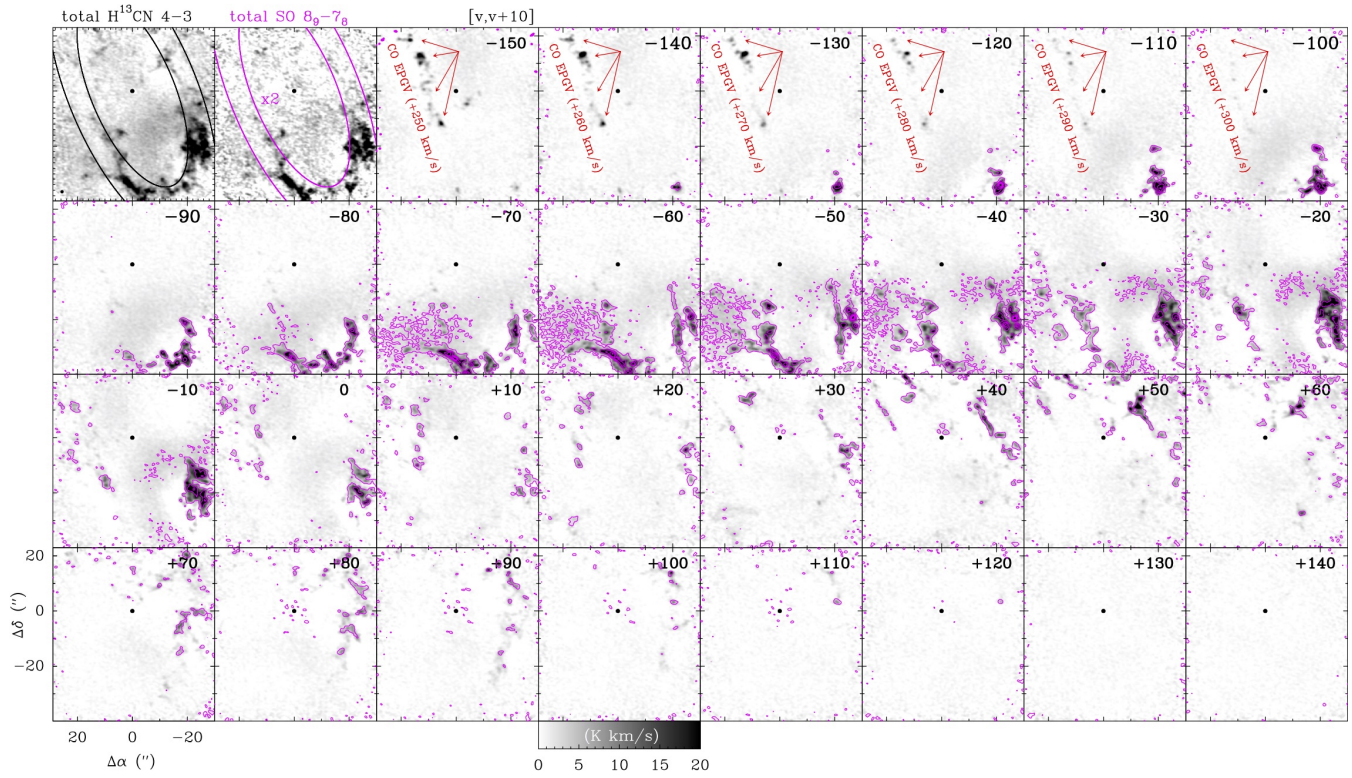

Fig. A.4. Nearly identical spatial distribution of $H^{13}CN$ ($J = 4$–3) and SO (8_9–7_8) from ALMA+TP observations (merged zero-spacing data). The *two top left panels* show total integrated line intensity maps. The other maps show $H^{13}CN$ ($J = 4$–3) (black images) and SO (8_9–7_8) (magenta contours) channel maps from $v_{LSR} = -150$ to $+150$ km s^{-1} in steps of 10 km s^{-1}. At all velocities, most $H^{13}CN$ and SO features spatially match (i.e., they belong to the same gas structure). The emission features seen at negative velocities without SO emission counterpart, however, do not arise from blue-shifted $H^{13}CN$ emission but from red-shifted ^{12}CO cloudlets. Sgr A* is at position (0″, 0″).

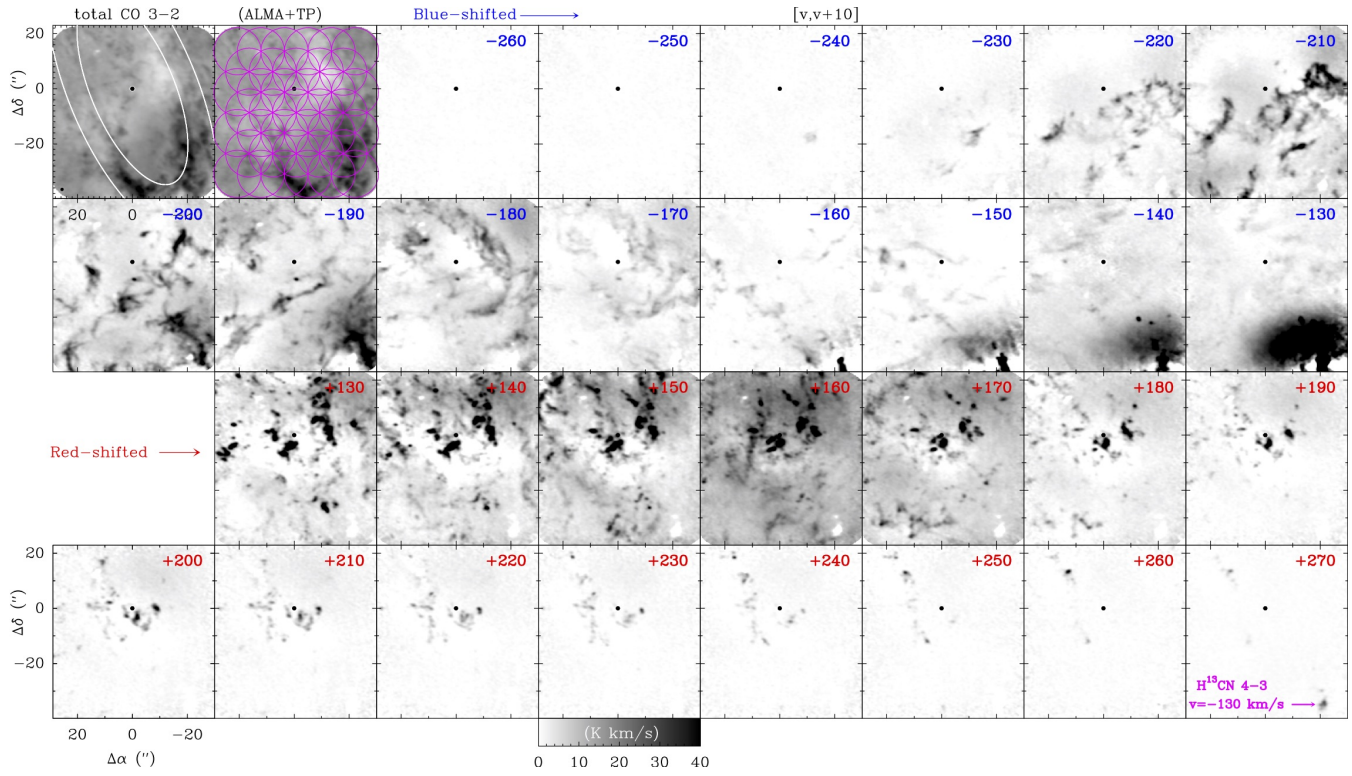

Fig. A.5. ALMA+TP observations ^{12}CO ($J = 3$–2) channel emission maps from $v_{LSR} = -260$ to -120 km s^{-1} (blue-shifted) and from $v_{LSR} = +130$ to $+280$ km s^{-1} (red-shifted) in steps of 10 km s^{-1}. Sgr A*, at position (0″, 0″), is displayed with a black dot.

Appendix B: High and extreme positive-velocity gas cloudlet spectral fitting

Table B.1. Gaussian fit parameters of ^{12}CO HPVG and EPVG cloudlets line emission (fit errors in parenthesis).

Cloudlet #	Offset[a] (arcsec)	Peak velocity (km s^{-1})	Line-width (km s^{-1})	Line-peak (K)
HPVG #1	(+2.3,−5.0)	155.5 (0.1)	37.9 (0.1)	13.6
HPVG #2	(−1.0,−2.7)	166.3 (0.1)	48.2 (0.1)	11.0
HPVG #3	(−7.2,+3.1)	170.0 (0.4)	28.9 (1.0)	10.2
HPVG #4	(+9.3,+1.7)	159.7 (0.1)	31.4 (0.2)	10.1
HPVG #5	(−6.1,+11.7)	161.6 (0.9)	28.0 (2.0)	6.8
HPVG #6	(−11.3,+10.7)	Multi-comp.		
EPVG #7	(−8.9,−0.3)	204.9 (0.1)	55.8 (1.1)	3.9
EPVG #8	(−2.3,−3.0)	Multi-comp.		
EPVG #9	(+16.5,+18.7)	242.1 (0.9)	23.8 (2.2)	3.7
EPVG #10	(+13.0,+13.0)	261.0 (0.5)	21.3 (1.2)	4.5
EPVG #11	(+5.6,−12.0)	254.6 (0.8)	28.6 (2.2)	2.1
EPVG #12	(+15.4,+1.1)	219.5 (1.3)	30.5 (3.0)	1.6
EPVG #13	(+8.9,+5.5)	228.8 (1.1)	27.8 (2.4)	2.2
EPVG #14	(−4.2,−2.5)	225.3 (1.1)	24.3 (3.1)	1.6
EPVG #15	(+3.7,−11.6)	212.4 (1.3)	31.7 (3.4)	1.4
EPVG #16	(+9.0,0)	222.6 (3.6)	40.0 (10.0)	1.6

Notes. [(a)]With respect to Sgr A*.